Doctoral Thesis

Reduction of Induced Electric Field in Human Body for Non-Radiative Wireless Power Transfer Systems

(非放射性無線電力伝送システムにおける人体内誘導電場の削減に関する研究)

2024

DUAN Xianyi

Contents

List of Figures

List of Tables

Chapter 1

Introduction

1.1. Background

Nonradiative wireless power transfer (WPT) systems have evolved significantly and now find applications across various industries, promising a revolution in electrical energy utilization. However, because these systems use electromagnetic fields (EMFs) for energy transfer, concerns have emerged regarding the potential risks associated with EMF exposure. Given the increasing prevalence of WPT systems, comprehending their safety implications is essential, particularly focusing on the interaction between humans and EMFs.

Human activities in proximity to these systems might disrupt their efficiency, whereas the EMFs generated can interact with biological tissues. Furthermore, WPT systems operate across a broad spectrum of frequencies, ranging from low to high. Low-frequency exposure (below 100 kHz) primarily results in electrostimulation due to induced electric fields within the body, whereas exposure to radiofrequency (above 100 kHz) may lead to thermal effects associated with temperature increase.

It is crucial to ensure optimal transmission efficiency, minimize human-system interaction, and address concerns about EMF exposure, particularly within diverse realistic scenarios.

1.1.1. Development of Wireless Power Transfer Technology

The roots of induction charging can be traced back to the pioneering work of eminent English physicist Michael Faraday in 1831 [1]. Heinrich Rudolf Hertz's discovery of radio waves in 1888 confirmed the electromagnetic propagation forecast by Maxwell [2]. Hertz's experiments demonstrated that electromagnetic waves could be produced in transmitter coils and wirelessly detected by a receiver coil [3]. Nikola Tesla's groundbreaking experiments in the late 1800s leveraged inductive coupling principles with Tesla coils, facilitating substantial alternating current (AC) [4]. Induction heating, which has been used since the early 1900s, has also been employed in induction cooking. In 2007, Soljačić *et al.* [5] theoretically demonstrated the feasibility of a four-coil configuration for wireless power transmission using the coupled mode theory, achieving a transfer of 60 watts with almost 40% efficiency over distances exceeding 2 m. Additionally, in 2011, Christopher *et al.* recreated Tesla's 1900 patent in miniature, demonstrating power transmission over 4 m with a coil diameter of 10 cm at a resonant frequency of 27.5 MHz and an effective efficiency of 60%. Currently, WPT technology is extensively applied in electric vehicle (EV) charging [6]–[8], consumer electronics [9], [10] , and biomedical implants [11], [12]. As the scientific community continues to refine this technology and address the associated challenges in high-efficiency and safety, future prospects for WPT remain promising.

In general, WPT can be classified into two primary types: radiative and non-radiative, each presenting distinct advantages in the realm of wireless power delivery. In radiative techniques, power is transferred by beams of electromagnetic radiation beyond about 1 wavelength (λ) of the antenna, like microwaves [13]. These techniques can transport energy longer distances but must be aimed at the receiver [14]. Proposed applications for this type include solar power satellites [15] and wireless powered drone aircraft [16].

The main focus of this thesis will solely be on non-radiative WPT techniques, which refers to energy transfer within the wavelength (λ) of the transmitter antenna. Extensive research has been conducted on various nonradiative WPT systems, each based on different coupling mechanisms, as follows:

- Inductive wireless power transfer (IPT): This technology transmits energy by inductively coupling the coils of a transmitter and receiver over a short distance using a magnetic field. Operating within the kilohertz range, this solution typically maintains a distance of no more than 40 mm between the transmitter and receiver. IPT technology is versatile and capable of transmitting energy from single watts to kilowatts [17];

- Capacitive wireless power transfer (CPT): CPT technology relies on capacitive coupling, utilizing transmitter and receiver capacitive electrodes shaped like metal plates. The transmitter system, powered by an alternating voltage source, generates an alternating potential displayed as a load on the receiver cover [18];
- Magnetic resonant coupling-type WPT (MRC-WPT): This technology operates through magnetic resonance coupling, employing resonant coils to facilitate wireless power transfer. Utilizing multiple coils, power transfer occurs through the interaction of magnetic fields between the transmitting and receiving unit. These units generally consist of resonant coils tuned to the same frequency, enabling efficient energy transfer over short to medium distances [19]. A significant advantage of MRC-WPT systems is their capacity to transfer power over larger air gaps compared with traditional inductive coupling.

IPT and CPT are typically suitable for relatively short distance energy transfer, while MRC-WPT excels in medium-range applications. Capacitive coupling increases energy transfer with heightened interplate capacitance and frequency. Consequently, this necessitates an increase in the total surface area of capacitors, an expansion in volume, and a requirement for high voltage across the capacitor plates [13]. For practical applications, magnetic resonance coupling and inductive coupling are considered the most suitable methods. This rationale underscores the in-depth examination of these methods in Chapters 3 and 4 of this thesis.

1.1.2. Related Standards and Guidelines

The rapid advancement of WPT technologies has led to the emergence of corresponding international standards and guidelines. They play an integral role in the development and safety of these technologies, establishing norms and best practices to ensure efficiency, interoperability, and compliance with safety regulations. These standards encompass various aspects of WPT, from power levels and frequency bands to limits of electromagnetic field exposure, providing a foundation for manufacturers, researchers, and regulatory authorities to coordinate efforts, encourage innovation, and uphold stringent safety protocols within the evolving realm of WPT technology.

Wireless Charging Standards

Numerous standards and guidelines have been introduced to address power transmission efficiency, maximum allowable transmission power, and frequency bands. These protocols are designed to ensure the safe and effective operation of WPT systems in industrial contexts.

One prominent standard, introduced by the Wireless Power Consortium in 2008, is the Qi Standard, primarily tailored for inductive charging within a 4 cm range [20]. This standard has become the leading choice for wireless power transmission, particularly in the smartphone industry. It stipulates power requirements in two categories: within 5W in the 110 to 205 kHz frequency range and up to 120W in the 80 to 300 kHz frequency range [21].

Another well-known wireless charging standard was introduced by the AirFuel Alliance in 2021, amalgamating the Alliance for Wireless Power (A4WP) and Power Matters Alliance [22]. The AirFuel standard employs magnetic resonance charging technology to power multiple devices simultaneously at speeds comparable to wired charging without necessitating precise placement on the charging surface. The AirFuel resonant standard requires 15 or 50W in the 6.78 MHz band, with a transmission distance request of 60 cm.

AirFuel emphasizes “magnetic resonance” technology, setting it apart from Qi’s “inductive” technology. While the former offers lower transmission efficiency, it enables wireless charging over slightly longer distances, offering greater flexibility. In contrast, the latter requires proximity, such as placing a smartphone on a charging pad, allowing contactless inductive charging with higher efficiency.

For WPT systems in EVs, stringent safety regulations are essential owing to the generation of high-power fields. In 2016, SAE International published SAE J2954, defining acceptable criteria for interoperability, electromagnetic compatibility, EMF, minimum performance, safety, and testing of wireless charging of light-duty electric and plug-in EVs. This standard categorizes four levels of charging power up to 22 kW, requiring more than 80% transmission efficiency at the 85 kHz frequency band [23]. Moreover, the International Electrotechnical Commission (IEC) publishes international standards IEC 61980-1, 2, and 3, specifically addressing the supply of devices for charging electric road vehicles wirelessly [24]–[26]. IEC 61980 categorizes power levels of up to 22 kW and limits the air gap to 24 cm. Another standard, ISO 19363, by the International Organization for Standardization (ISO), outlines the specifications and functionality of onboard vehicle equipment facilitating magnetic field WPT for charging EV traction batteries [27]. This standard, tailored for use in passenger cars and light-duty vehicles, covers various aspects, including the transferred power, ground clearance of the EV device, and more.

In addition, several countries, such as China, Japan, Europe, and the USA, have comprehensive testing methods and management solutions for wireless charging devices [28].

Human Exposure Standards and Guidelines

Various regulatory bodies have established guidelines and standards to prevent human overexposure to EMFs. The International Commission on Nonionizing Radiation Protection (ICNIRP) [29] and the IEEE International Committee on Electromagnetic Safety [30] are two international bodies mentioned by the World Health Organization. The ICNIRP guidelines set two types of limits: the basic restriction (BR) and the reference level (RL). These are indicated as

Table 1.1 Basic restrictions in different guidelines/standards for general public exposure, f in Hz.

Quantity	Induced electric field; E_{ind} [V/m]		Localized SAR [W/kg]		Whole-body SAR [W/kg]
Spatial Average	$2 \times 2 \times 2$ mm^3 (cube)		1g	10g	-
Frequency range	1 Hz–3 kHz	3 kHz–10 MHz	100 kHz–6 GHz		
Value	0.4	$1.35 \times 10^{-4} f$	1.6 (head & torso)	2 (head & torso)	0.08
			4 (limbs)		

Table 1.2 Reference levels in in different guidelines/standards for general public exposure, f in Hz

Frequency range	Magnetic flux density [T]	Magnetic field strength [A/m]	Electric field strength [V/m]
1–8 Hz	$4 \times 10^{-2}/f^2$	$3.2 \times 10^4/f^2$	5
8–25 Hz	$5 \times 10^{-3}/f$	$4 \times 10^3/f$	5
25–50 Hz	2×10^{-4}	1.6×10^2	5
50–400 Hz			$2.5 \times 10^2/f$
400 Hz–3 kHz	$8 \times 10^{-2}/f$	$6.4 \times 10^4/f$	
3 kHz–10 MHz	2.7×10^{-5}	21	8.3×10^{-2}
10–30 MHz	-	0.073	-

the dosimetry reference limit (DRL) and exposure RL (ERL) in the IEEE C95.1 standard. BRs concern internal-field quantities associated with adverse health effects and are characterized by certain reduction factors. Conversely, RL signifies the permissible external-field strength without the presence of a human body for practical compliance assessments. The limitations of exposure based directly on physical quantities linked to established health effects are termed basic restrictions, which can be challenging to assess. Hence, they are conservatively derived from the RL. RL is generally derived under the assumption that a standing human is exposed to a uniform field in a worst case scenario [31]. However, in specific scenarios with relatively strong local exposure, such as holding a mobile phone close to the head, the RL may not be applicable [32]. In such cases, a compliance assessment with the basic restrictions should be directly evaluated.

Low-frequency exposure (below 100 kHz) primarily causes electrostimulation owing to the induced electric field in the body, while radiofrequency (RF) exposure (above 100 kHz) leads to thermal effects associated with a rise in body temperature due to power absorption. For near-field exposure scenarios at frequencies around the MHz range, compliance estimation was evaluated using the specific absorption rate (SAR) rather than the induced electric field. The BRs and RLs, listed in Tables 1.1 and 1.2, serve as optimization limits in this thesis, depending on the frequency. However, consideration of implantable devices falls beyond the scope of this thesis.

1.1.3. Previous Related Studies and Research Scope

Human-system Interaction

In previous studies, it was observed that the proximity of the human body to WPT systems could cause a mismatch between the input impedance of the transmitting and receiving coils, resulting in reduced transmission efficiency [33]. The transmitting power of a WPT system can fluctuate owing to changes in the input impedance caused by human-system interaction, as evidenced in previous research [34]. Other related studies have highlighted how minimizing impedance-mismatch conditions could impact compliance assessments for human protection [35]–[37].

Reducing Leakage of Electromagnetic Field

Because WPT operates via electromagnetic fields, reducing its impact on the human body becomes crucial. Sometimes, the most restrictive factor reported is human protection rather than electromagnetic interference with nearby electric or electronic devices [38], [39]. Frequency-splitting phenomena owing to the presence of multiple coils also raise concerns in WPT systems [40]. Additionally, at low frequencies, the human body acts as a poor conductor [41]. Consequently, the electric field on the body surface must be perpendicular to it, inducing an electric field in the human body owing to the accumulation of electric charge on the surface of the body [42].

Increasing magnetic field leakage can compromise human safety. Methods such as compensation topology and passive shielding have been proposed to reduce the leakage magnetic field of WPT systems [43]–[45]. Although these studies have largely focused on the compliance assessment aspects of WPT systems, they have not thoroughly investigated the effects of the human body on WPT performance.

Initially, ferrite cores, such as E- and U-type cores, were proposed to reshape the magnetic path and reduce leakage, which are primarily used in EV applications [46]. However, owing to their high cost, large weight, and poor misalignment tolerance, alternate ferrite cores with different structures and materials were suggested. For instance, a circular core structure was proposed to reduce the core thickness and magnetic flux leakage [47], [48]. Additionally, variations such as the double-D quadrature [49], H-shaped [50], and tripolar pad core [51] structures were introduced to address misalignment issues. Tapered cores were explored owing to their good alignment tolerance and coupling coefficients [52]. Furthermore, some studies [53]–[55] have discussed the use of optimal core thickness and coil shape to enhance system performance and misalignment resilience. However, these studies concentrated on the system design and paid limited attention to the adverse effects of magnetic field leakage on humans.

Numerical Dosimetry Study

The presence of a human body significantly impacts the transfer performance of WPT systems [56]. Assessing the induced electric field strength in the human body is a common method used to evaluate EMF safety in WPT systems [57]. Numerical dosimetry, which frequently employs anatomically realistic human voxel models [58] based on magnetic resonance imaging data [59]–[61], is utilized to explore electromagnetic field effects during WPT, particularly concerning human health and safety. Numerous studies have focused on WPT-oriented numerical dosimetry. Laakso *et al.*[62] and Arduino *et al.* [63] investigated exposure to the magnetic fields of EV wireless charging systems. S. Park *et al.* [64] calculated the internal electric fields induced by a four-coil MRC-WPT system in the human body. Additionally, other studies evaluated the exposure of misaligned WPT systems to the human body and assessed the induced field amounts due to time-varying magnetic fields generated by various WPT systems [37], [65]. These studies extensively evaluated the variations in the induced electric field within the human body using different human models [66], postures [67], [68], and body positions [42], [60], [69]. Some studies have specifically focused on determining the coupling factor to establish the relationship between the peak in-situ electric field and the applied nonuniform magnetic field [70], [71].

This study is dedicated to the comprehensive safety evaluation of WPT systems, emphasizing their implications for the human body. This research focuses on two key points: human interaction with WPT systems and the health risks associated with EMF exposure. It explores innovative techniques, such as loop structures, aimed at reducing human exposure during WPT operations. Additionally, within realistic scenarios, this study investigates the feasibility of using composite cores to shield against leakage magnetic fields, safeguarding the health of bystanders in EV charging applications. The ultimate goal of this study was to enhance WPT technology for efficient utilization without compromising human health.

1.2. Content of Thesis

This study focuses on simulating the performance and EMF distribution of a nonradiative WPT system while computationally evaluating the physical quantities in a human model exposed to this system. It introduces two designs, the grounded loop and composite core, aimed at different coupling types in the WPT system. The primary goal is to establish efficient and safe systems for various realistic scenarios. The motivations for this study are as follows:

1. Minimizing human interaction with WPT systems to enhance system safety while maintaining high efficiency across different application scenarios. This study utilizes full-wave simulations and a simplified homogeneous human body model to analyze the system's performance.

2. Mitigating the health risks associated with EMF exposure by reduce the leakage electromagnetic field. Calculations of physical exposure quantities have been conducted in a numerical human model under the magneto-quasi-static assumption.

3. Carrying out compliance assessments of the proposed systems, considering various limitations of international guidelines and standards.

The thesis comprises the following chapters:

Chapter 1 introduces the background and motivation of this study.

Chapter 2 explains the models and computational methods used in this study. It begins by presenting the theoretical WPT system model and two human body models. The chapter then details the full-wave simulation using COMSOL software and describes the scalar potential finite difference (SPFD) method for computing the induced electric field strength in numerical human models. The SAR equation, utilizing the electric field obtained in SPFD, is also presented.

Chapter 3 proposes a grounded loop in the four-coil MRC-WPT system to reduce the external electric field and enhance the transmission efficiency. It investigates the system's performance under the influence of the human body via simulations. Calculations of the induced electric field strength and SAR in a worst case exposure scenario for the numerical human body model are conducted. Additionally, compliance assessments are performed, considering various international codes and standards' limitations.

Chapter 4 explores the effectiveness of using a composite magnetic core in an inductive WPT system for EV to reduce external magnetic field emissions and improve transmission efficiency. Three different shapes of intermediate insert blocks are considered for the core design. The chapter evaluates the efficiency and leakage magnetic field strength of these core structures against a coreless system. It investigates the induced electric field strength concerning the vehicle model and discusses the effect on the human model under perfectly aligned and misaligned conditions. For compliance assessment, a common exposure scenario involving a human model standing near an EV was considered.

Chapter 5 summarizes the main conclusions of this study.

Chapter 2

Modeling and Methodology

2.1. Overview

First, the theoretical model and the equivalent circuit of the WPT system and its details are introduced. The commercial software COMSOL Multiphysics (COMSOL Inc., Burlington, MA, USA) [72] is used, employing a field-circuit co-simulation approach to evaluate the transmission efficiency of the WPT system. Following that, a detailed description of the two-stage computation method used how to compute physical quantities will be provided [42]. In the first stage, magneto-quasi-static computation has been performed for the magnetic field distribution. In the second stage, the physical quantities are computed using the quasi-static dosimetry method-scalar potential finite difference (SPFD), which has been widely used in previous research on human exposure [73]. The proposed computational approach has been validated by intercomparison with [62] and [74]. In addition, When the human body is exposed to radio waves at frequencies above 100 kHz, some of the energy is absorbed by the body and converted into heat. The specific absorption rate (SAR) equation is the most commonly used equation to express the amount of heat absorbed [29].

This chapter describes the WPT system model, homogeneous axial-symmetric human model, anatomical human body model, and the associated computation methods.

2.2. Models

2.2.1. Theoretical Wireless Power Transfer System Model

According to Oersted's law, a steady current produces a magnetic field around it. The magnetic flux passing through the receiver will be expressed as:

$$\phi = \iint_S \boldsymbol{B} dS \tag{2.1}$$

where ***B*** is the magnetic flux density generated by the transmitter and *S* is the area of the receiver coil surface. Since the time-dependent current of the transmitter coil produces magnetic flux variation in the receiver coil, electromotive force is induced in the receiver coil, which we can derive by applying Faraday’s law [1]:

$$\boldsymbol{\varepsilon} = -\frac{d\phi}{dt} \tag{2.2}$$

Self-inductance *L* is the property of the circuit when its own magnetic field is opposing the current change in the circuit. Self-inductance of the coil can be defined as:

$$L = \frac{N\phi}{I} \tag{2.3}$$

where *N* is the number of turns, ϕ is magnetic flux and *I* is the current of the coil [3]. By combining (2.11) and (2.12) , the following equation can be obtained:

$$\boldsymbol{\varepsilon} = -L\frac{dI}{dt} \text{ or } -M\frac{dI}{dt} \tag{2.4}$$

where *M* is the mutual inductance of two coils. Obviously, the EMF induced on the coil is directly proportional to the self- or mutual-inductance of the coils and the rate at which the current is changing [5]. Another representation of mutual inductance is the following:

$$M = k\sqrt{L_1 L_2} \tag{2.5}$$

where k is the coupling factor and $L_{1/2}$ is the inductance of the transmitter/receiver coil. The coupling factor defines the grade of the coupling, i.e., how much flux of the total flux actually penetrated the receiver coil. It can have a value from 0 to 1 (from zero to perfect coupling).

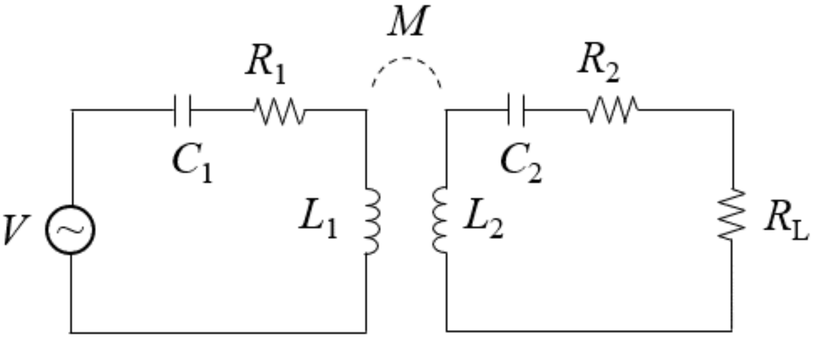

Figure 2.1 Simplified representation of the two-coil coupling WPT system.

Figure 2.1 depicted a simplified representation of the WPT system. The transmitter/receiver coil can be represented by series inductor $L_{1/2}$ and resistances $R_{1/2}$. The R_1 and R_2 represent the resistances due to the ohmic and radiation losses of the transmitter and receiver [75]. The R_L is the load resistance. The function M represents the mutual inductance. Capacitors C_1 and C_2 are used to tweak the transmitter and receiver resonance to the desired frequency [76]. V is the input voltage and V_{RL} is the output voltage. When the transmitter and receiver are in resonance, the transmission efficiency of the WPT system can be calculated using the following equation based on the coupled-mode theory [5], [77].

$$P_{R_L} = \frac{V_1^2 \omega^2 M^2 R_L}{(R_1(R_2 + R_L) + \omega^2 M^2)^2} \tag{2.6}$$

The overall transmission efficiency is then can be depends on the transmission frequency, mutual inductance, coils' parasitic resistances and load resistance, as shown in the following equation:

$$\eta = \frac{\omega^2 M^2 R_L}{R_1(R_2 + R_L)^2 + \omega^2 M^2 (R_2 + R_L)} \tag{2.7}$$

where the transmission efficiency η is defined as a ratio of input to output power, ω is the operating frequency of the system, M represents the mutual inductance, The resistances R_1, R_2 and R_L represent the resistance of the transmitter coil, receiver coil and the load, respectively.

Q factor (Quality factor) is defined by the ratio of the inductance to the resistance of the coil. A higher Q factor means a lower energy loss and so better transmission efficiency. It can be defined as:

$$Q = \frac{\omega L}{R} \tag{2.8}$$

where L is the inductance of the coil, R is its resistance and ω is the operating frequency of the system. Obviously, Q factor increases when the operating frequency increases. However, when it reaches its peak values, it will decrease as the operating frequency continues to rise. What is more, a higher Q factor means a narrower bandwidth, which results in dropped coupling efficiency and the need of a tuning circuit.

Now the maximum transfer efficiency is defined by the following equation:

$$\eta = \frac{k^2 Q_1 Q_2}{(1 + \sqrt{1 + k^2 Q_1 Q_2})^2} \tag{2.9}$$

where k is the coupling factor between two coils and Q_1 and Q_2 are the quality factors of the transmitter and receiver coils.

2.2.2. Human Models

Simplified Homogeneous Human Body Model

The human-body models adopted are shown in Figure 2.5. A simplified homogeneous human body model was adopted from the IEC62233 standard [78]. Its height and maximum diameters were 1.528 and 0.35 m, respectively, which approximated the size of an adult human body. In addition, the dielectric properties of the homogeneous model were set to two-thirds of those of a muscle, an approach which is often used to represent the average electrical properties of a human body [35]. This model is used to evaluate the human-system interaction in Chapter 3.

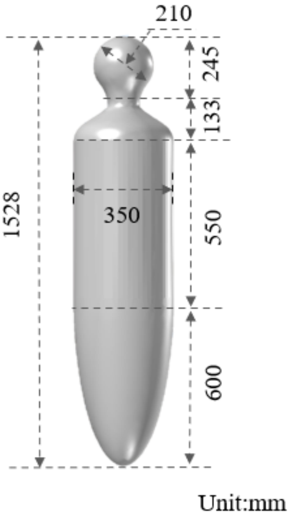

Figure 2.2 Simplified homogeneous human body model.

Anatomical Human Body Model

Anatomical body models have been widely adopted in dosimetry studies and have been considered by ICNIRP to relate RL with BR. In the present work, the Japanese adult male model, TARO [58], shown in Figure 2.5, developed by the National Institute of Information and Communication Technology, Tokyo, Japan, was adopted for a detailed assessment of the exposure dose in a realistic human body. This voxel-based model consisted of 51 tissues and organs, and its spatial resolution was 2 mm. The dielectric properties of the tissues were obtained from the four-Cole–Cole dispersion model [79]. This model is used in Chapter 3 and 4. While other research has explored various human models, including those for children model [80] and female model [58], [81], this thesis exclusively employs TARO model to calculate exposure doses.

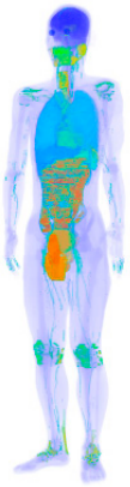

Figure 2.3 Anatomical human body model.

2.2.3. Vehicle Cabin Model

A simplified vehicle cabin model based on the Toyota Motor Corporation Prius [82] for which the WPT system is implemented, is depicted in Figure 2.4. The vehicle body is assumed to be placed in free space. As the relative permeability of a window is 1, glass windows in the vehicle were not considered in the evaluation because of their negligible impact on the magnetic field [74]. The vehicle body is fabricated using aluminum with 2.0 mm thickness.

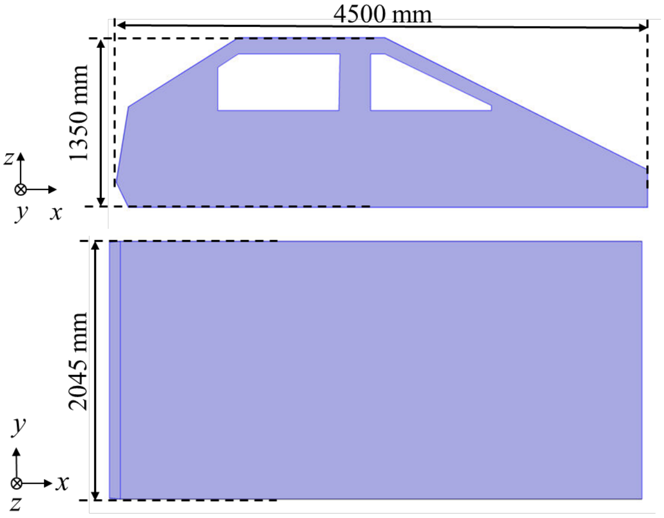

Figure 2.4 Cross-section of the electric vehicle (EV) cabin model (xz-plane and xy-plane).

2.3. Methods

Quasi-static approximations are often used in the frequency range below about a few hundred kHz without validation. In contrast, full-wave analyses are typically used for frequencies above 10 MHz. Based on the wide distribution of operating frequencies of WPT systems and the purpose of this study, one full-wave analysis method and one quasi-static analysis method are considered.

2.3.1. Finite Element Method

Finite element analysis is a method used to solve general systems of partial differential equations (PDEs), which are expressed in a discrete and approximate form [42]. This method allows us to solve field problems defined by complex geometries and constraints. Therefore, it enables the definition of more governing equations, allowing us to deal with coupled physical problems in electromagnetics. The analysis can be divided into three parts:

- Pre-processing: Development of the model (geometry, mesh, material, solver).
- Solver: Solution of linear or nonlinear systems.
- Post-processing: Elaboration and management of results.

In FEM, Failure to correctly impose all these conditions can result in the solving algorithm not converging to the solution or producing inaccurate results. Boundary conditions and sources

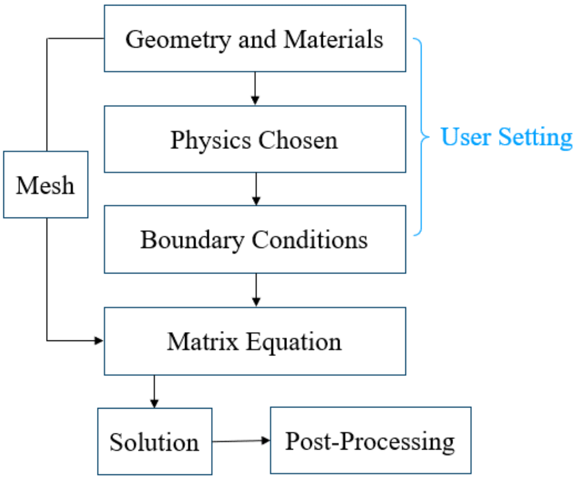

Figure 2.5 Basic steps to perform a finite element analysis in COMSOL Multiphysics®.

become the known terms vector. When the unknown values are found (usually scalar and vector potentials), it is possible to obtain the field functions by applying approximate differential operators (curl, gradient, divergence). The simulations conducted in this study were performed using COMSOL 5.6a and 6.0.

In classical physics, electromagnetic phenomena are described by a system of four partial differential equations, synthesized by James Clerk Maxwell. Maxwell unifies the Ampere law (2.10), the Faraday-Lenz law (2.11) and the Gauss laws of electric (2.12) and magnetic fields (2.13).

$$\nabla \times \boldsymbol{H} = \sigma \boldsymbol{E} + \frac{\partial(\varepsilon \boldsymbol{E})}{\partial \boldsymbol{t}} \tag{2.10}$$

$$\nabla \times \boldsymbol{E} = -\frac{\partial(\mu \boldsymbol{H})}{\partial \boldsymbol{t}} \tag{2.11}$$

$$\nabla \times \boldsymbol{E} = 0 \tag{2.12}$$

$$\nabla \times \boldsymbol{H} = 0 \tag{2.13}$$

In these equations, $\boldsymbol{E}$ is the electric field [V/m], $\boldsymbol{H}$ is the magnetic field [A/m], ε is the ratio of electric displacement to the electric field intensity (electric permittivity) [F/m], μ is the magnetic permeability [H/m] and σ is the electric conductivity.

Maxwell-Ampere's law and Faraday's law can be combined into a second-order wave equation by substituting the curl values of one equation into the other. In other words, the system formed by these two first-order equations represents an electromagnetic wave. These equations are topological relations that impose the geometry of the fields and their evolution over time. Therefore, starting from the following relations, we can obtain a general expression of the radiated fields:

$$\nabla \cdot \boldsymbol{B} = \boldsymbol{0} \tag{2.14}$$

$$\nabla \times \boldsymbol{H} = \boldsymbol{J} + \frac{\partial \boldsymbol{D}}{\partial \boldsymbol{t}} \tag{2.15}$$

$$\boldsymbol{J} = \sigma \boldsymbol{E} \tag{2.16}$$

$$\nabla \times \boldsymbol{E} = -\frac{\partial \boldsymbol{B}}{\partial \boldsymbol{t}} \tag{2.17}$$

In these equations, $\boldsymbol{E}$ is the electric field [V/ m], $\boldsymbol{D}$ is the electric flux density [C/m], $\boldsymbol{B}$ is the magnetic flux density [W/bm^2], $\boldsymbol{H}$ is the magnetic field [A/m] and $\boldsymbol{J}$ is the electric current density [A/m^2]. These equations are most important equations for electromagnetic wave.

Equation (2.14), (2.15), and (2.17) are also can be writing as integral form, as the following:

$$\oint_s \boldsymbol{B} \cdot nds = \boldsymbol{0} \tag{2.18}$$

$$\oint_c \boldsymbol{H} \cdot dl = \boldsymbol{I} + \oint_c \frac{\partial \boldsymbol{D}}{\partial \boldsymbol{t}} \cdot ds \tag{2.19}$$

$$\oint_c \boldsymbol{E} \cdot dl = -\oint_c \frac{\partial \boldsymbol{B}}{\partial \boldsymbol{t}} \cdot ds = -\frac{\partial \boldsymbol{\phi}}{\partial \boldsymbol{t}} \tag{2.20}$$

Here, ϕ is the magnetic flux through the closed contour *C*.

Assume that the material properties are homogeneous and isotropic (this assumption is valid only to obtain a general expression of propagation, but we will have to make into account the inhomogeneity for the propagation into the tissues). The permeability μ can then be taken outside of the time derivative in Faraday's law (2.2) and the take the curl of this equation:

$$\nabla \times (\mu^{-1} \nabla \times \boldsymbol{E}) = -\frac{\partial (\nabla \times \boldsymbol{H})}{\partial \boldsymbol{t}} = -\frac{\partial}{\partial \boldsymbol{t}} \left(\sigma \boldsymbol{E} + \frac{\partial (\varepsilon \boldsymbol{E})}{\partial \boldsymbol{t}} \right) = -\sigma \frac{\partial \boldsymbol{E}}{\partial \boldsymbol{t}} - \varepsilon \frac{\partial^2 \boldsymbol{E}}{\partial \boldsymbol{t}^2} \tag{2.21}$$

Collecting terms on one side gives as the following:

$$\nabla \times (\mu^{-1} \nabla \times \boldsymbol{E}) + \sigma \frac{\partial \boldsymbol{E}}{\partial \boldsymbol{t}} + \varepsilon \frac{\partial^2 \boldsymbol{E}}{\partial \boldsymbol{t}^2} = \boldsymbol{0} \tag{2.22}$$

A similar derivation gives the following equation in terms of the magnetic field as shown in the following equation:

$$\nabla \times (\nabla \times \boldsymbol{H}) + \sigma\mu \frac{\partial \boldsymbol{H}}{\partial \boldsymbol{t}} + \varepsilon\mu \frac{\partial^2 \boldsymbol{H}}{\partial \boldsymbol{t}^2} = \boldsymbol{0} \tag{2.23}$$

While in free space, $\sigma = 0, \mu = \mu_0$, and $\varepsilon = \varepsilon_0$. The equation for the electric field can be put on the form:

$$\nabla \times (\nabla \times \boldsymbol{E}) + \varepsilon_0\mu_0 \frac{\partial^2 \boldsymbol{E}}{\partial \boldsymbol{t}^2} = \boldsymbol{0} \tag{2.24}$$

Or it can be written as:

$$\nabla \times (\nabla \times \boldsymbol{E}) + \frac{1}{c_0{}^2} \frac{\partial^2 \boldsymbol{E}}{\partial \boldsymbol{t}^2} = \boldsymbol{0} \tag{2.25}$$

where the $c_0 = \frac{1}{\sqrt{\varepsilon_0\mu_0}}$.

Considering the Gauss's law (2.3) in the free space and together with the vector identity:

$$\nabla \times \nabla \times \boldsymbol{E} = \nabla \cdot (\nabla \cdot \boldsymbol{E}) - \nabla^2 \boldsymbol{E} = -\nabla^2 \boldsymbol{E} \tag{2.26}$$

gives the following, and perhaps more familiar, form of the wave equation:

$$\nabla^2 \boldsymbol{E} - \frac{1}{c_0{}^2} \frac{\partial^2 \boldsymbol{E}}{\partial \boldsymbol{t}^2} = \boldsymbol{0} \tag{2.27}$$

and similarly gives the following form for the magnetic field:

$$\nabla^2 \boldsymbol{H} - \frac{1}{c_0{}^2} \frac{\partial^2 \boldsymbol{H}}{\partial \boldsymbol{t}^2} = \boldsymbol{0} \tag{2.28}$$

It is possible to derive a second-order wave equation by means of the magnetic vector potential. To do so, start by assuming the temporal gauge,

$$\boldsymbol{E} = -\frac{\partial \boldsymbol{A}}{\partial \boldsymbol{t}} \tag{2.29}$$

together with the definition of the vector potential,

$$\boldsymbol{B} = \nabla \times \boldsymbol{A} \tag{2.30}$$

and substitute them into Maxwell–Ampère's law:

$$\nabla \times (\mu^{-1}(\nabla \times \boldsymbol{A})) = -\sigma\frac{\partial \boldsymbol{A}}{\partial \boldsymbol{t}} - \frac{\partial}{\partial \boldsymbol{t}}(\varepsilon\frac{\partial \boldsymbol{A}}{\partial \boldsymbol{t}}) = -\sigma\frac{\partial \boldsymbol{A}}{\partial \boldsymbol{t}} - \varepsilon\frac{\partial^2 \boldsymbol{A}}{\partial \boldsymbol{t}^2} \tag{2.31}$$

Note that this formulation is for a time-independent material. For a time-dependent material, the permittivity cannot be taken outside of the time derivative.

2.3.2. Computer Method

Scalar Potential Finite Difference (SPFD) Method

There are various analysis methods such as the moment method and the finite element method in EM computation. In this study, we analyzed using the SPFD method [83], which has a comparatively small computational capacity and is suitable for computation of EM fields in anatomical numerical models with inhomogeneous properties. The EM field in the analytical region can be solved by Maxwell's equations discretized in the time and the spatial domain.

The SPFD method sets the branch current instead of the loop current. The unknowns in this method are the scalar potential values at the nodes (corners) of each voxel. Branch currents flowing along the edges of the voxels are then derived from the potential difference between neighboring nodes and the conductivity of the voxels. The branch current calculation also takes into account magnetic vector potential of the applied magnetic field. By applying Kirchhoff's current law at all nodes, simultaneous equations are thereafter established. The potential is subsequently solved iteratively. The electric field along the side of the voxel is obtained by dividing the difference of the potentials between the nodes of the voxel by the distance across the nodes and then adding the vector potential,

$$\sum_{n=1}^{6} S_n \phi_n - \left(\sum_{n=1}^{6} S_n \right) \phi_0 = j\omega \sum_{n=1}^{6} (-1)^n S_n l_n A_{0n} \tag{2.32}$$

$$\boldsymbol{E} = -\nabla \varphi - j\omega \boldsymbol{A}_{0n} \tag{2.33}$$

where S_n, ϕ_n, l_n, ω, and $\boldsymbol{A}_{0n}$ denote the edge conductance derived from tissue conductivity, scalar potential, length between nodes, angular frequency, and magnetic vector potential, respectively.

Specific Absorption Rate (SAR) Equation

Squared values of $\boldsymbol{E}$, $\boldsymbol{H}$, and I are considered for time or spatial integration, or where summation of multiple frequencies is applied. The following equation is an example of the spatial average of $\boldsymbol{E}$ over a volume V:

$$E_{Spatial\_average} = \sqrt{\frac{1}{V}\int_{v} |\boldsymbol{E}|^2 \, dv} \tag{2.34}$$

where V is the volume of the integration ($V = \int_v \, dv$).

Dielectric properties of biological tissues or organs are generally considered as dielectric lossy material and magnetically transparent because the relative magnetic permeability (μ_r) is 1.Therefore, the SAR is usually can be related to the electric field at a point by the following equation:

$$SAR = \frac{\sigma|\boldsymbol{E}|^2}{\rho} \tag{2.35}$$

where $\boldsymbol{E}$ is the internal electric field, and the parameters σ and ρ are the conductivity and mass density, respectively.

The dielectric properties of the tissues were determined with 4-Cole–Cole dispersion model, where the upper frequency at which the measured data were considered is 20 GHz [84]. For frequencies higher than 20 GHz, the expansion of the Cole–Cole dispersion model was verified using the measurement and parametric model in [85]. The variation in the temperature rise in tissue thickness is more dominant than in dielectric properties [86]. In addition, heating factors for multi-layered models with skin tissue were consistent with those for models consisting of the epidermis and dermis tissue instead of the skin at 30 GHz [87]. Therefore, in this study, the tissue dielectric and conductivity parameters of dry skin were modeled using a four-layer Cole–Cole dispersion model based on [84].

Definition of Physical Quantities

SAR is used as a basic restriction in the two international standards and guidelines [29], [30], defined as spatially averaged values: whole-body average SAR and SAR_{10g}. The whole-body average SAR is the total power absorbed in the whole body divided by the body mass. 10-g SAR is defined as the total absorbed power averaged over 10-g, corresponding to a cube with a side length of 21.5 mm.

$$SAR_{10g} = \frac{(Total\ power)_{V_{10g}}}{(Totla\ mass)_{V_{10g}}} = \frac{\int_{V_{10\mathrm{g}}} \sigma|\mathbf{E}|^2 dv}{\int_{V_{10\mathrm{g}}} \rho dv} \tag{2.36}$$

$$\text{Whole-body average SAR } = \frac{(Total\ power)_{WB}}{(Totla\ mass)_{WB}} = \frac{\left[\int_{WB} \sigma|\mathbf{E}|^2 dv\right]_{WB}}{\int_{WB} \rho dv} \tag{2.37}$$

Note that the cubic averaging shape for the computation of 10-g SAR, the algorithm specified in [88] was applied to clarify the treatment of the air region and the pinna.

Chapter 3

Reduction of Leakage Electric field with Grounded Loop

3.1. Overview

This study investigates the reduction of leakage electric field and human interaction with MRC-WPT systems using grounded loops. The performances of the two WPT systems with and without the presence of a human body were first determined using the finite-element method (FEM) in COMSOL Multiphysics 5.6a (COMSOL Inc., Burlington, MA, USA). Next, the induced electric field in a human body was computed for two WPT systems using the scalar-potential finite difference (SPFD) method. This study also compares the SAR and the induced electric fields in the human-body model when the WPT is used with and without the grounded loop. Finally, the related SAR limits of the ICNIRP guidelines for the general public are discussed in the worst-case exposure scenario.

3.2. Models and Methods

3.2.1. Geometric Structure of the MRC-WPT System

This chapter discusses the variations of an MRC-WPT system using different resonators. As shown in Figure 3.1, in this study we adopted a four-coil MRC-WPT system. The transmitter and receiver are composed of a single-loop coil and a resonator. The distance between the single-loop coil and resonator was set to 4 cm, where the quality factor of the two resonators is most equal.

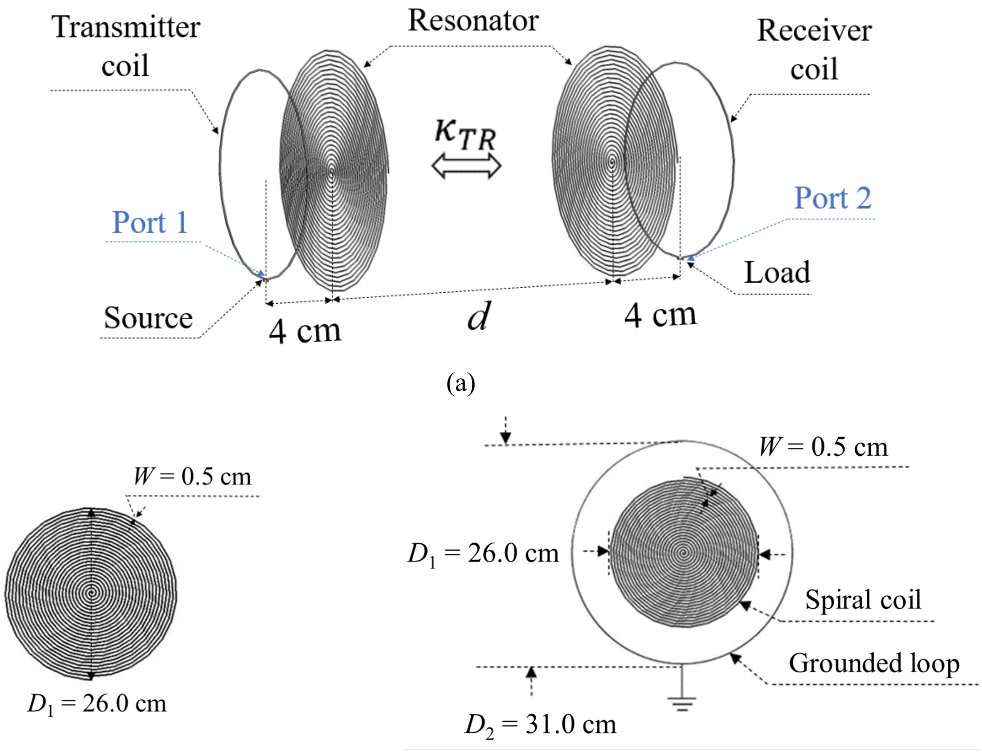

(a)

(b)

(c)

Figure 3.1 Geometrical structure of the proposed MRC-WPT system. (a) Four-coil MRC-WPT system. (b) Non-grounded resonator. (c) Proposed resonator with a grounded loop.

Two types of resonators were considered: a conventional resonator and our proposed resonator structure. The conventional resonator consisted of a spiral coil, referred to here as a non-grounded resonator. The proposed resonator aims to reduce the coupling between the WPT system and the human body, using a grounded single-loop coil around the spiral coil. The spiral coil and grounded loop were coaxially located on the same plane. This resonator is hereafter referred to as a "grounded resonator" for simplicity. To achieve a grounded condition, we set the potential at the bottom end of each loop to zero to simulate a grounded state. It should be noted that this is an idealized scenario. The receiver structure of the MRC-WPT system was identical to that of the transmitter [89]. The geometric parameters of the spiral resonator were determined using its self-resonant frequency and quality factor [90]. κ_{TR} represents the coupling coefficient between the transmitter (denoted as T) and receiver (denoted as R). Resistance is connected to the receiving coil, imitating the load. All coils used in this study were made of 1-mm-diameter copper wire [75].

Although in realistic scenario, the WPT system with loop structure is able to fit many frequencies [91], [92], the working frequency was set to 13.56 MHz in this study since this is a promising frequency for WPT applications in industrial, scientific, and medical fields [37], [93], [94].

When the transmitter and receiver are in resonance, the transmission efficiency of the WPT system can be calculated using Equation (3.1) based on the coupled-mode theory [5], [77].

$$\eta = \frac{\frac{\mathit{\Gamma}_W {\kappa_{TR}}^2}{{\mathit{\Gamma}_R}^2 \mathit{\Gamma}_T}}{\left[\left(1 + \frac{\mathit{\Gamma}_W}{\mathit{\Gamma}_R}\right) \frac{{\kappa_{TR}}^2}{\mathit{\Gamma}_T \mathit{\Gamma}_R}\right] + \left(1 + \frac{\mathit{\Gamma}_W}{\mathit{\Gamma}_R}\right)^2} \tag{3.1}$$

where κ_{TR} is the coupling coefficient, $\mathit{\Gamma}_{T/R}$ denotes the attenuation rates of the transmitter and receiver due to ohmic and radiation losses, and $\mathit{\Gamma}_W$ refers to the attenuation rates of the load [5]. Thus, efficient transmission occurs when the MRC-WPT system operates in a strongly coupled system, i.e., ${\kappa_{TR}}^2/\mathit{\Gamma}_\mathrm{T}\mathit{\Gamma}_\mathrm{R} > 1$. The variables $\mathit{\Gamma}_\mathrm{T}$ and $\mathit{\Gamma}_\mathrm{R}$ can be calculated using Equation (3.2).

$$\mathit{\Gamma} = \omega_0/2Q \tag{3.2}$$

where ω_0 is the resonant angular frequency of the resonator and $Q = \omega_0 L/R$ is the quality factor of the transmitter or receiver.

Figure 3.2 shows the equivalent lumped-circuit model of the four-coil MRC-WPT system [5]. The signal power of the transmitter part generated by voltage source V_S is transferred to the receiver part at resonant frequency f_0 and is then delivered to load R_L. The transmitter and receiver can be represented by series inductors (L_1 and L_2) and resistances (R_1 and R_2). The parameter R_1 and R_2 represent the resistances due to the ohmic and radiation losses of the transmitter and receiver [75]. The function $M = \kappa_{TR} (L_1 \times L_2)^{1/2}$ represents the mutual inductance. Capacitors C_1 and C_2 are used to tweak the transmitter and receiver resonance to the desired frequency [76].

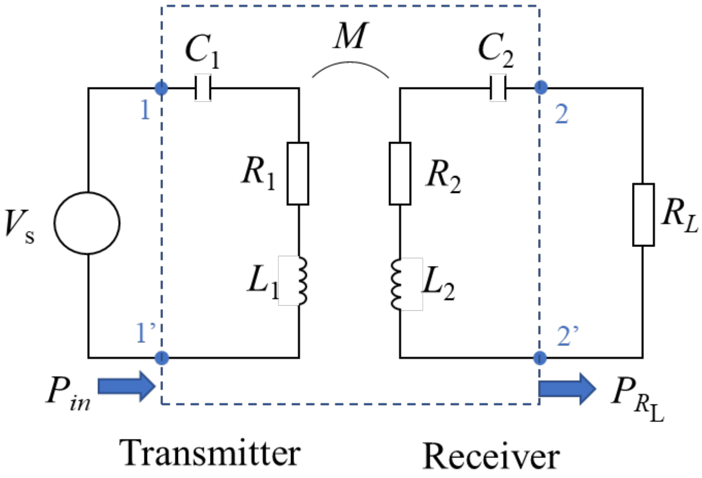

Figure 3.2 Equivalent lumped-circuit model of the four-coil MRC-WPT system.

In this study, the voltage source is applied without considering impedance matching [95]. Therefore, the transmission efficiency η of the entire WPT system (blue dashed box in Figure 2) can be calculated as the ratio between the actual input power at port 1–1′, i.e., P_{in}, and actual output power P_{RL}, which is expressed as follows:

$$\eta = \frac{P_{R_L}}{P_{in}} \times 100 \tag{3.3}$$

3.2.2. Human Body Models and Exposure Scenario of the Simulation

Exposure Scenarios

The WPT system was installed at the body model’s chest level, as shown in Figure 3.3 (a). The separation between the grounded loops and the body model was 2 mm. Different locations of the

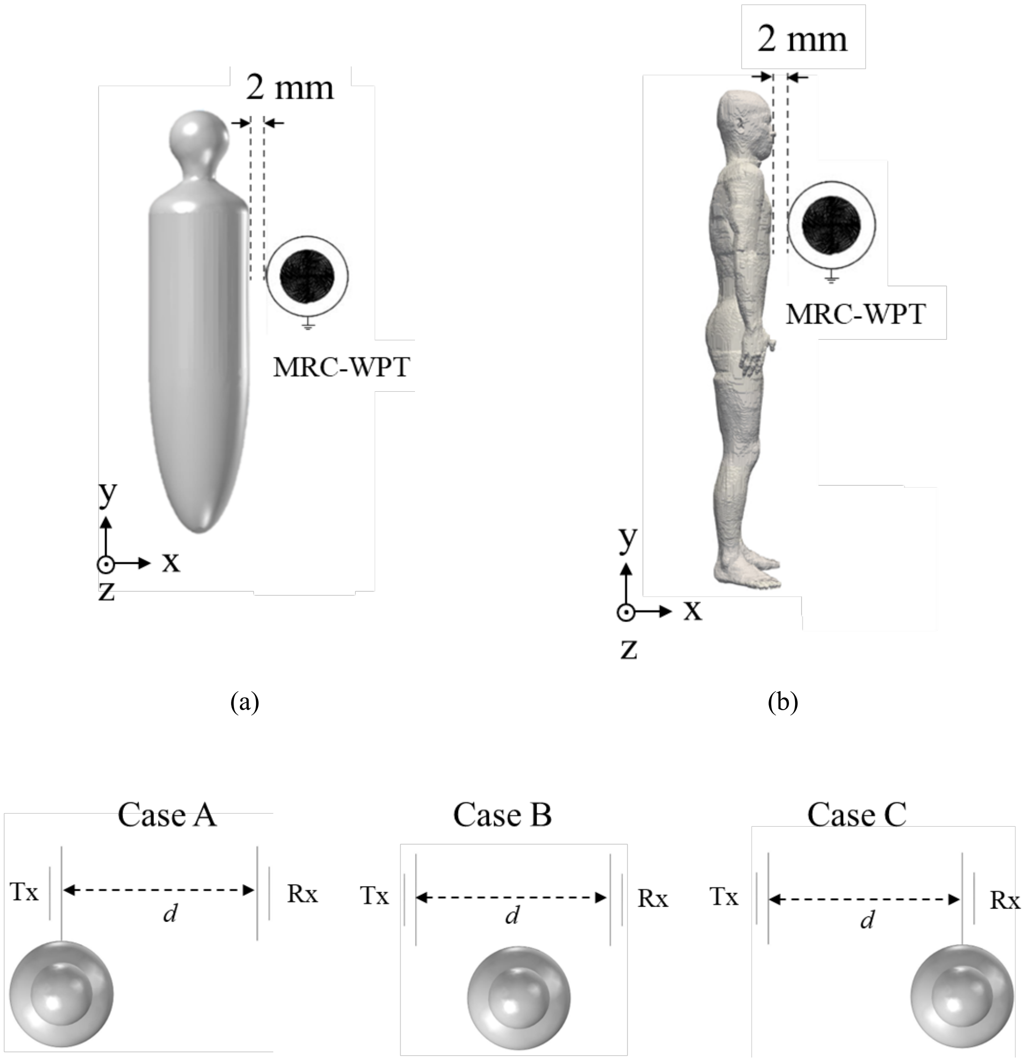

(a)

(b)

(c)

Figure 3.3 The MRC-WPT with respect to the (a) homogeneous body and (b) TARO models. (c) Top view of the MRC-WPT and homogenous human model.

human-body model were considered in this study to analyze the mutual interaction between the human body and the WPT system. Three exposure cases, corresponding to three body locations relative to the WPT system, were considered for each WPT system. These are Case A (human model standing near the transmission unit), Case B (human model standing near the center part of the system), and Case C (human model standing near the receiving unit), where *d* is the distance between the transmitter and receiver, as shown in Figure 3.3 (c).

Simulation of Mutual Interaction

The finite-element method in COMSOL commercial software was used [72] to evaluate the mutual interactions between the human body and the MRC-WPT system. The circuit shown in Figure 3.2 was coupled using the COMSOL field-circuit co-simulation method to evaluate the transmission efficiency [72], [96], [97]. The simulation domain was a 1.2-m-diameter sphere, which enclosed the WPT system. An absorbing boundary condition was applied to the surface of the sphere. The coil materials were set to copper, which came with the software.

The parameters L, ω_0, and R were calculated using the frequency domain solver of the full-wave electromagnetic simulation package COMSOL. Compensation capacitors C_1 and C_2 were used to make the transmitter and receiver resonant at the desired frequency [76], in which the lumped inductances were numerically extracted using COMSOL Multiphysics 5.6a. The theoretical maximum transmission efficiency was obtained by adjusting the load impedance R_L [5]. The dependence of transmission efficiency on the transmission distance d for the matched state of the MRC-WPT system with grounded and non-grounded resonators was evaluated using Equation (3.3) based on the processes mentioned above. The stray magnetic field was also evaluated at the same time.

To simulate the human-system interaction, the simplified homogeneous human body, as shown in Figure 3.3 (a), was adopted in this analysis due to the difficulties in handling fine-resolution voxel-based body models. Tetrahedral meshes were used to discretize the simulation domain, and the software automatically determined the mesh sizes. We compared the results using finer settings, and the calculations indicated that the applied discretization resolution did not affect the results.

Simulation of Exposure Dose in the TARO Model

To assess the impact of the exposure dose in a realistic anatomical human-body model (TARO), the magnetic vector potential values were first calculated using the stray magnetic fields simulated using COMSOL in the absence of a body model [68], [73]. Next, the induced electric field was computed by means of an in-house-developed solver using the SPFD method. The convergence was accelerated using the geometric multigrid method [73]. The magnetic vector potential values were used as the source of the SPFD computation, which represented the scenario of exposure to the external WPT magnetic field. The applicability of this two-step approach was confirmed by [42].

The presence of the human body did not perturb the external magnetic field distribution, and the displacement current could be neglected at low frequency. Subsequently, the specific absorption rate (SAR) in each voxel was evaluated from the electric field using the "mid-ordinate" algorithm [98]. The spatial-average SAR value was determined by averaging the local SAR with more than 10 g of cubical volume using the method described in [65]. The peak spatial-average SAR (*ps*SAR) averaged over 10 g of tissues and the whole-body average SAR were computed. All computational results were normalized to an input power of 1 W in the MRC-WPT system.

3.3. Results

3.3.1. Validation of the MRC-WPT System Computation

We compared the calculated transmission efficiency with our experimental results [89] to validate our computational model. The experiment result was expressed as Equation (3.4) [99],

$$\eta_{Ex} = \frac{10^{\frac{|S_{21}|}{10}}}{1-10^{\frac{|S_{11}|}{10}}} \times 100\ [\%] \tag{3.4}$$

and the COMSOL results were evaluated using Equation (3.3). In the experimental study, the resonant frequency of the WPT system was set to 10 MHz. Therefore, the operating frequency of the computational model was adjusted to 10 MHz. This may not violate the generality principle as the frequency and coil length are inversely proportional to each other.

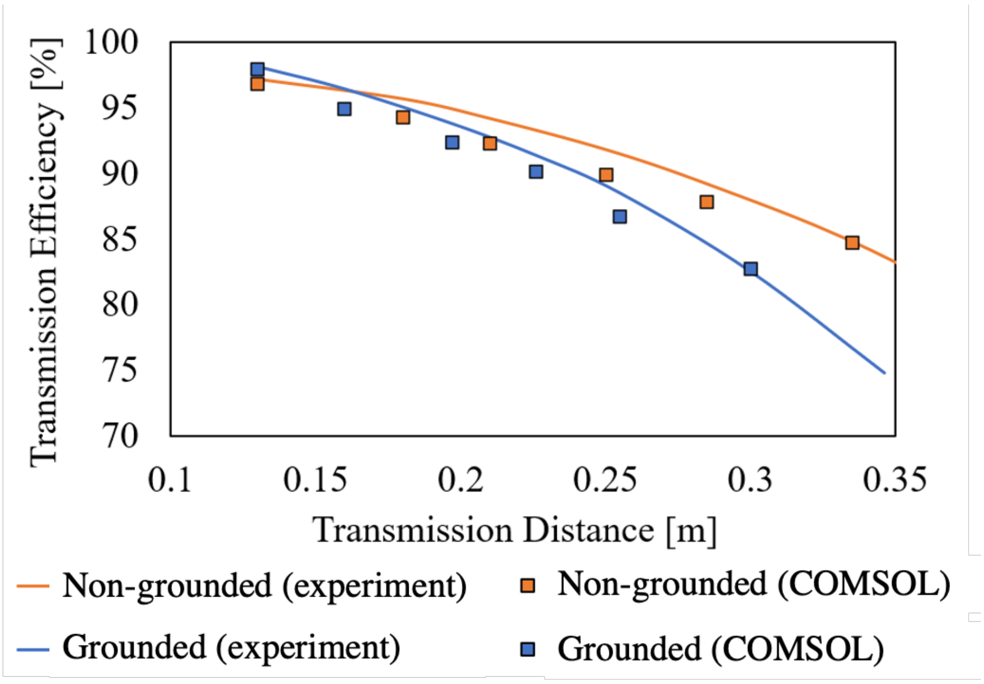

Figure 3.4 Experimental validation of transmission efficiency of MRC-WPTs' two resonator types (10 MHz).

Figure 3.4 shows the differences between the computation and measurement results. The transmission efficiency was within approximately 5% of the difference (the change was most significant when using non-grounded resonators with a transmission distance of 0.21 m), which validated the computational methods used in the current study.

3.3.2. Interactions between the Human Body and MRC-WPT System

The frequency characteristics of the S parameter of the two WPT systems, with and without the presence of a human body, are shown in Figure 3.5. Assuming a source and load impedance of 50 **Ω**, the WPT reflection coefficient (S_{11}) for a grounded resonator, both with and without a human-body model, consistently demonstrated lower values compared to the WPT with a non-grounded resonator. Additionally, the bandwidth characteristics of the two resonator types exhibited notable distinctions.

Table 3.1 enumerates the S_{11} values for both WPT systems, with and without a human model, precisely at their resonant frequencies set to 13.56 ± 0.01 MHz. Notably, when considering the human model, the S_{11} values for the WPT with a non-grounded resonator exhibited variability within the range of -8.16 to -6.06 dB. In stark contrast, the S_{11} values for the WPT with a grounded resonator showcased a significantly narrower range, varying from -14.97 to -14.1 dB. This nuanced exploration of the S parameter highlights the impact of human presence on the reflection characteristics of the WPT systems, emphasizing the efficacy of a grounded resonator in mitigating reflection coefficients.

Table 3.1 S_{11} (dB) of the two WPT systems with and without a human-body model at resonant frequency.

Resonator Type	Frequency (MHz)	Without Human Body	With Human Body
Non-grounded	13.55	−8.16	−6.06
Grounded	13.57	−14.97	−14.10

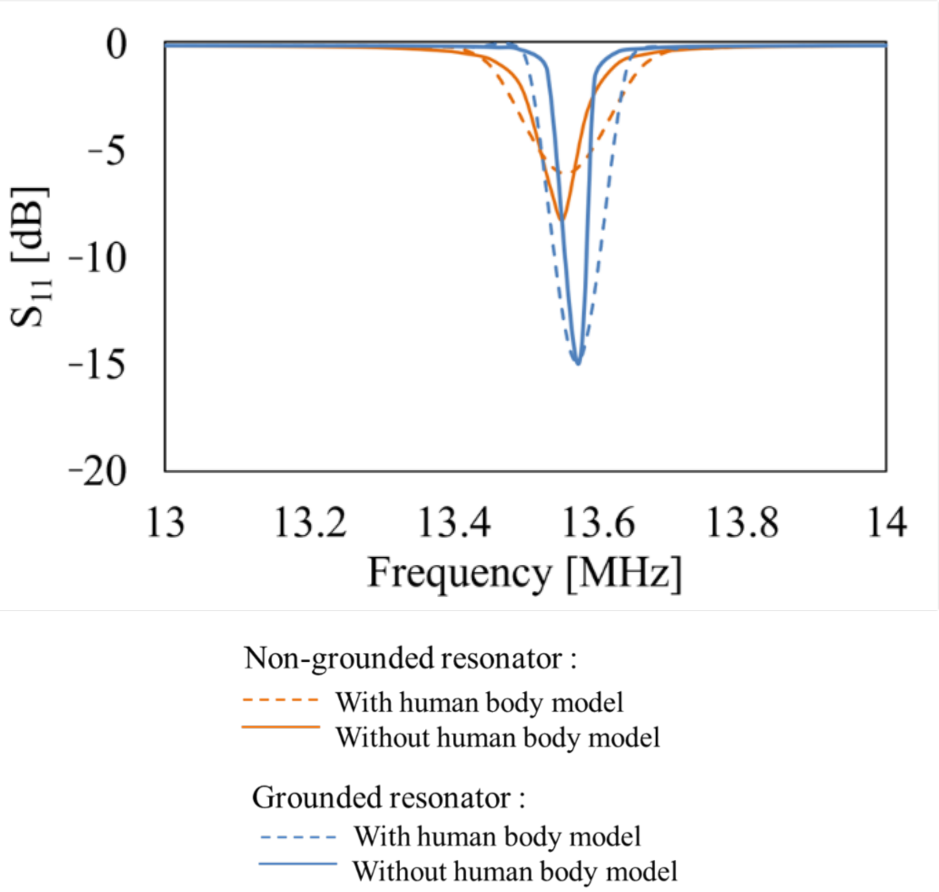

Figure 3.5 S parameter (S_{11}) for the two resonators.

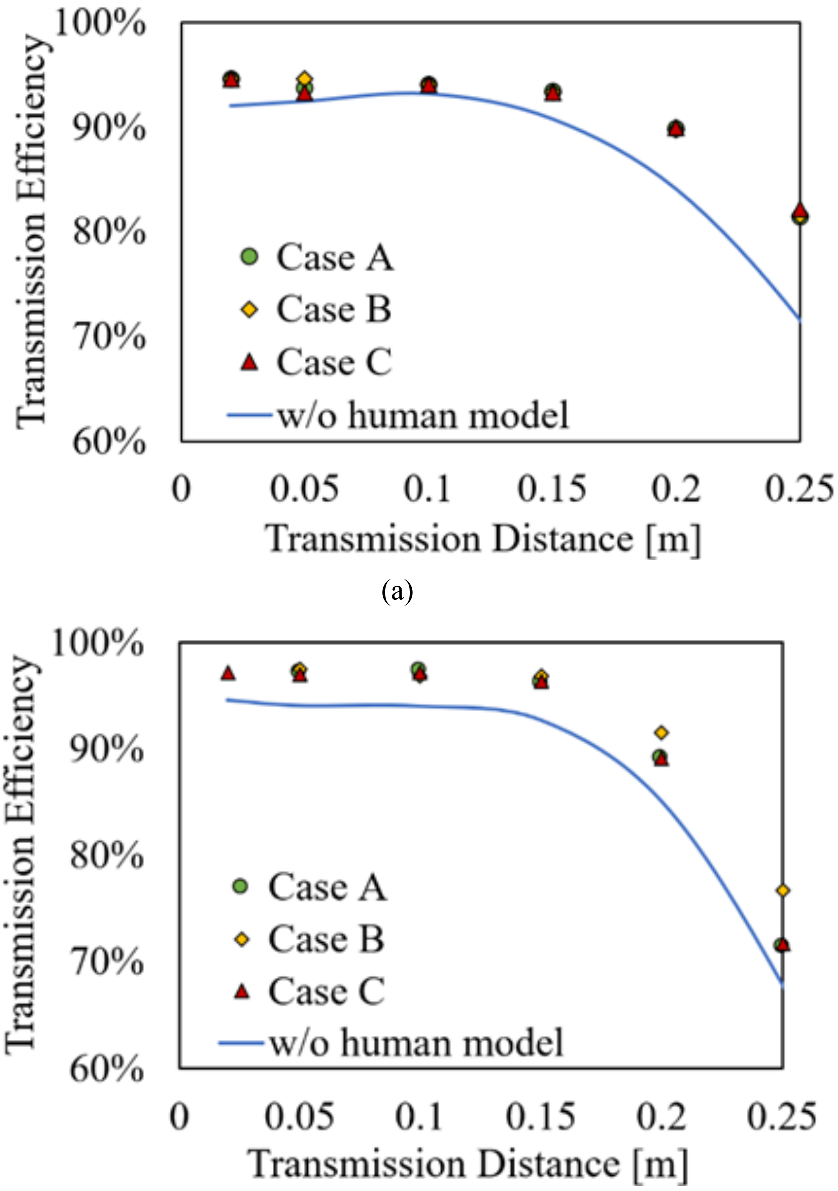

(a)

(b)

Figure 3.6 Dependence of transmission efficiency of (a) non-grounded and (b) grounded resonator with *d* at 13.56 MHz.

Figure 3.6 shows the transmission efficiencies at different transmission distances *d*. The solid curves in Figure 3.6 show that the transmission efficiency gradually decreased with increasing the transmission distance *d* without considering the human model. In addition, the transmission efficiency of the MRC-WPT system with a grounded resonator exhibited slightly better performance than the non-grounded resonator at $d < 23$ cm. Next, we considered the effects of the presence of a human body on the transmission efficiencies of the two types of MRC-WPT

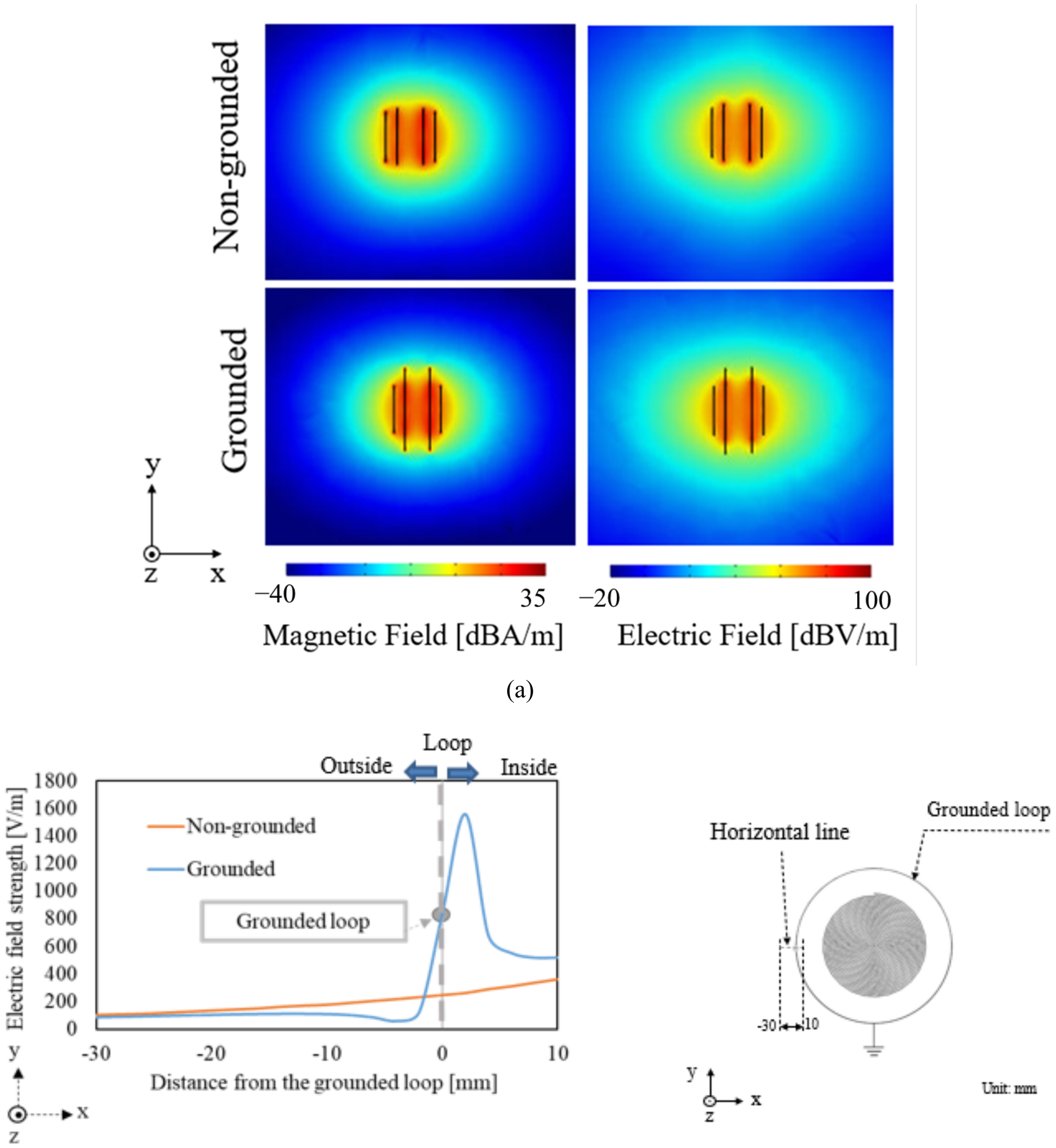

(a)

(b)

Figure 3.7 Electromagnetic-field distribution of two 13.56-MHz MRC-WPT systems without a human model when the input power is 1 W and the transmission distance $d = 9$ cm. (a) Electric and magnetic field distributions around the WPT systems. (b) Electric field on a horizontal line. The gray circle illustrates the location of the grounded loop.

systems at different body locations with the increase in the transmission distance. The markers in Figure 3.6 showed small increases in the transmission efficiencies when the human body was close to both systems. For example, at $d < 10$ cm, the variations in transmission efficiencies were marginal for the two systems. However, the influence of the human body reduced the transmission efficiency by up to 10 percentage points at a maximum distance of 25 cm. Altogether, the variation in transmission efficiency is marginal at different body locations (i.e., cases A, B, and C), mainly due to the size of the human body being larger than the transmission distance.

The quality factors and coupling coefficients of the two MRC-WPT systems with and without a human-body model at $d = 9$ cm are listed in Table 3.2. The presence of a human body caused an approximately 3% variation in the quality factor in the non-grounded resonator, whereas it was around 0.5% in the grounded resonator. For the coupling coefficients, the presence of a human body caused a nearly 11.4% variation in the non-grounded resonator and a 26.2% approximated variation in the grounded resonator.

Table 3.2 Quality factor and coupling coefficient of the transmitter in the MRC-WPT systems for the two types of resonators. $d = 9$ cm.

Resonator	Quality factor		Coupling coefficient	
	Without human body	With human body	Without human body	With human body
Non-grounded	215.4	222.7	0.128	0.144
Grounded	234.2	235.3	0.146	0.198

The electric field distributions of the two MRC-WPT systems were also calculated. Figure 3.7 (a) shows that the grounded loop concentrated the electromagnetic fields around the MRC-WPT systems. A section of the data line is shown in Figure 3.7 (b) to illustrate the electric field's strength inside and outside the grounded loop. The origin of the coordinates in Figure 3.7 (b) was set to a point in the grounded loop. In addition, Figure 3.7 (b) confirmed that the electric field outside the grounded loop was reduced compared with that in the WPT system with a non-grounded resonator. The electric field distribution results were also consistent with those derived from S_{11} [100].

3.3.3. Exposure Doses in the TARO Model

Induced Electric Field

An in-house-developed SPFD solver was used to calculate the induced electric field in the TARO model. This analysis utilized a 1-W transmission power, applied to two distinct resonators operating at 13.56 MHz. The transmitter-receiver separation, denoted as '*d*,' was fixed at 9 cm, representing the distance conducive to maximum system efficiency. The spatial relationships between the MRC-WPT system and TARO are visually depicted in Figure 3.3. Furthermore, Figure 3.8 provides detailed visualizations of the induced electric field and local Specific Absorption Rate (SAR) distributions. Across all scenarios, pronounced hotspots manifested around the chest region in the TARO model, notably the body part in closest proximity to the WPT system.

Table 3.3 Maximum induced electric field strength (V/m). RD refers to relative difference.

Model Displacement	Non-Grounded	Grounded	RD
Case A	3.44	1.94	43.6%
Case B	3.22	2.02	37.3%
Case C	2.98	1.85	37.9%

Of particular significance, the effectiveness of the grounded resonator in diminishing the induced electric field within TARO was observed. The maximum induced electric field strengths for simulated cases (A, B, and C) are systematically detailed in Table 3.3. Critically, the induced electric fields across various body model locations within the grounded resonator exhibited a notable degree of comparability. Notably, the grounded resonator, integrated into the MRC-WPT system, showcased a capacity to reduce internal doses within the TARO model.

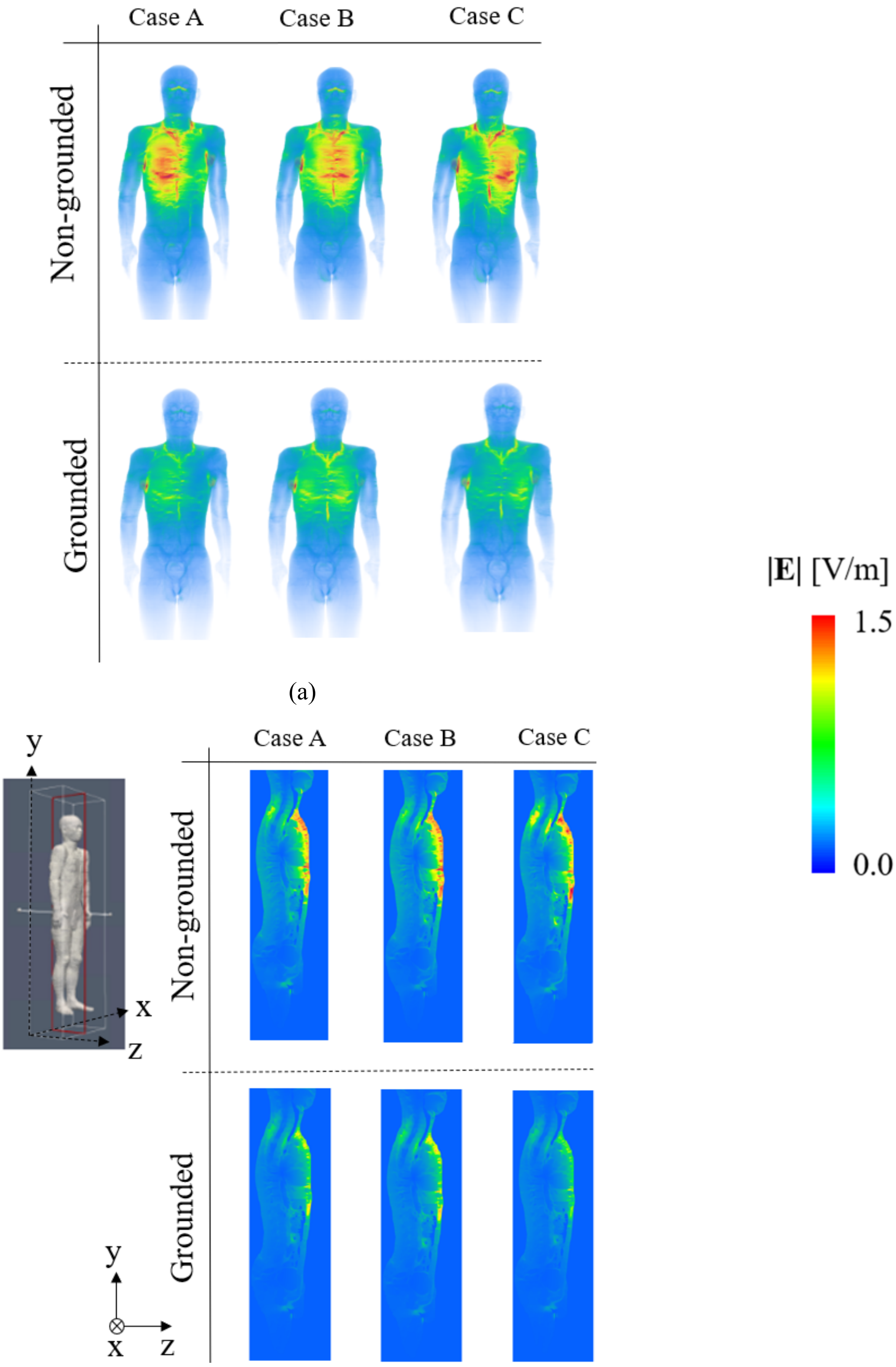

(a)

(b)

Figure 3.8 Induced electric field distribution on TARO. (a) Body surface. (b) Cross-sectional plane of input power 1 W, and transmission distance $d = 9$ cm.

Specific Absorption Rate

The local Specific Absorption Rate (SAR) within the TARO model was assessed using a 1-W transmission power for two types of resonators operating at 13.56 MHz. This evaluation employed the SPFD method, mirroring the approach used for the induced electric field analysis. The distance (*d*) between the transmitter and receiver was set at 9 cm, representing the distance at which the system achieves maximum efficiency. The local SAR distributions, depicted in Figure 3.9 revealed distinct hotspots around the chest region in the TARO model, aligning with the induced electric field distribution—consistent with the proximity of the chest to the WPT system.

Reductions in SAR within the TARO model were observed when utilizing a grounded resonator in the WPT system. Notably, the maximum peak spatial SAR (*ps*SAR) and whole-body average SAR for all simulated cases (A, B, and C) are detailed in Table 3.4 and

Table 3.5. respectively. The SAR values across different body model locations in the grounded resonator demonstrated comparability. These outcomes suggest that the grounded resonator configuration in the MRC-WPT system effectively diminished internal doses within the TARO model. The SARs of the different body model locations in the grounded resonator were

Table 3.4 Maximum $psSAR_{10g}$ (W/kg). RD refers to relative difference.

Model Displacement	Non-Grounded	Grounded	RD
Case A	1.88 E-4	0.57 E-4	69.7%
Case B	2.04 E-4	0.67 E-4	67.1%
Case C	1.35 E-4	0.50 E-4	63.0%

Table 3.5 Whole-body average SAR (W/kg). RD refers to relative difference.

Model Displacement	Non-Grounded	Grounded	RD
Case A	8.34 E-6	2.87 E-6	65.6%
Case B	7.94 E-6	3.48 E-6	56.1%
Case C	6.12 E-6	2.39 E-6	61.0%

comparable. Results shows that the grounded resonator of the MRC-WPT system reduced the internal doses in the TARO model.

Remarkably, the grounded resonator exhibited an approximately 60% reduction in both *ps*SAR and whole-body average SAR, confirming a substantial decrease in human body exposure doses achieved through the implementation of the proposed grounded resonator.

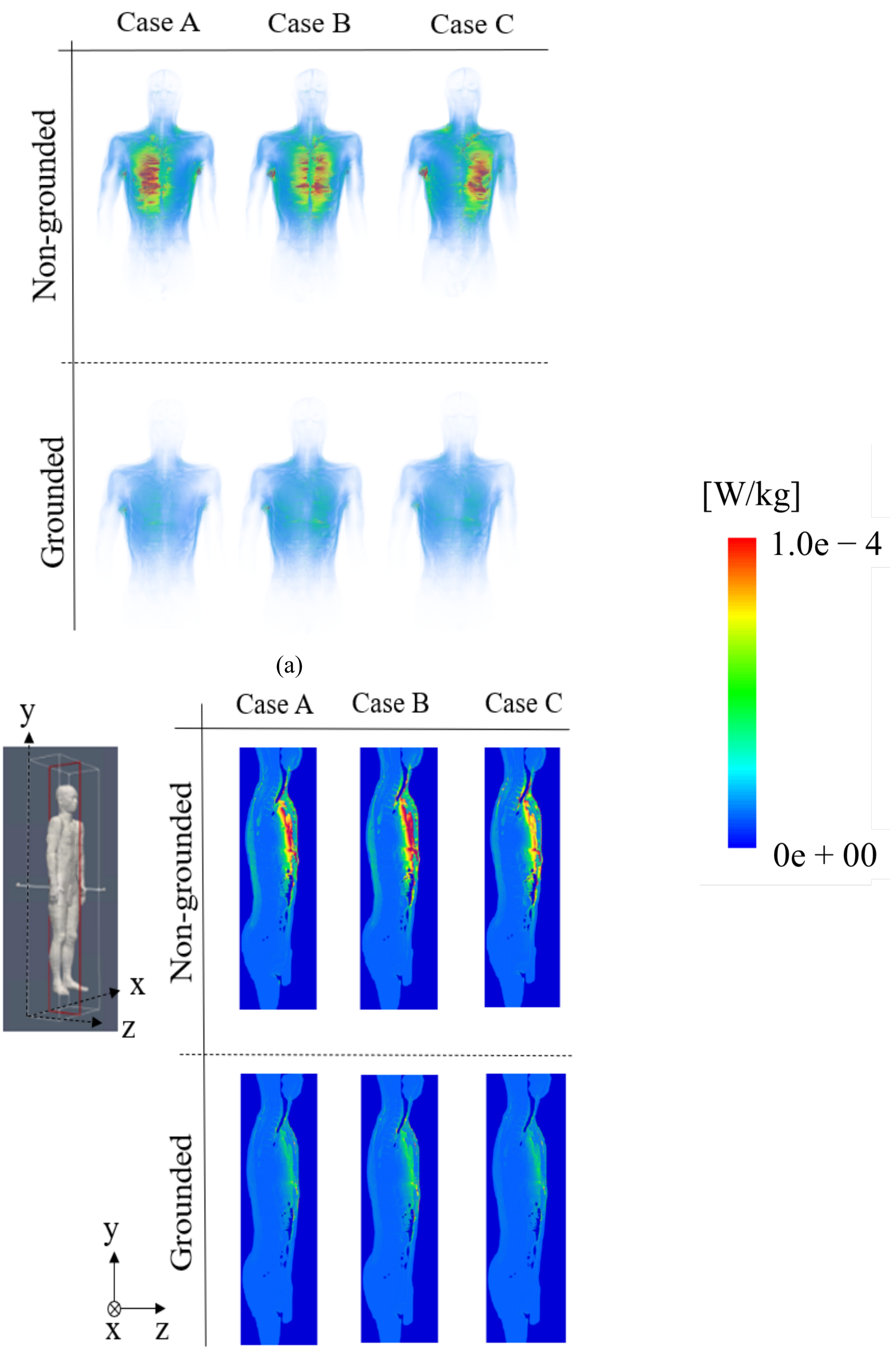

(a)

(b)

Figure 3.9 Local SAR distributions on TARO. (a) Body surface. (b) Cross-sectional plane of input power 1 W, and transmission distance $d = 9$ cm.

3.4. Discussion

The narrower peak for the grounded resonator is a clear indicator that the *Q* value is higher than that of the non-grounded resonator, indicating an increase in transmission efficiency. The simulation results in Figure 3.5 suggest that the grounded loop could mitigate the reflection coefficient changes and suppress the electric field strength. The results of *S*-parameter implied that the grounded resonator suppressed the interaction of the human model with the WPT performance. As a result, with the presence of human models, the bandwidths of the curves in Figure 3.5 became wider, indicating reduced quality factors with human models.

Results in Figure 3.6 shows that the transmission efficiency of both two systems decreased with increasing the transmission distance *d*, this is because of the decreasing coupling coefficient between the transmitter and receiver. The variation in transmission efficiency is marginal at different body locations (i.e., cases A, B, and C), which mainly occurred because the size of the human body was larger than the transmission distance. In general, the proposed grounded resonator increased the quality factors and coupling coefficients of the MRC-WPT system, which led to slightly improved transmission efficiency compared with the system with a non-grounded resonator. The results listed in Table 3.1 and Table 3.2 indicate that the presence of a human body significantly affects the coupling coefficients of both WPT systems in short-range transmission. The presence of a human body model results in a decrease in *S* parameter, an increase in the quality factor, and a higher coupling coefficient. This could be attributed to the alteration in the direction of the surrounding electromagnetic field caused by the presence of the human model, thus leading to an overall improvement in transmission efficiency.

The simulation results shown in Figure 3.8 and Figure 3.9 indicate that the induced electric field and SAR in the human body were reduced in the MRC-WPT system with a grounded resonator. This was mainly caused by the grounded loop that suppressed the leakage of the electromagnetic field around the MRC-WPT system, resulting in interaction with the human-body model.

According to the ICNIRP guidelines, the general public's *ps*SAR and whole-body average SAR limits are 2 and 0.08 W/kg, respectively [29], [30]. The results listed in Table 3.4 and

Table 3.5 show that the whole-body average SAR was more restrictive than *ps*SAR in the MRC-WPT system and the exposure scenarios considered in the present study. By applying the *ps*SAR limit, the maximum permissible input power of the grounded MRC-WPT was 40.0 kW, whereas it was 14.8 kW for the non-grounded MRC-WPT system. By applying the whole-body average SAR limit, the maximum permissible transmission power values were found to be 33.5 and 13.1 kW for the MRC-WPT systems with grounded and non-grounded resonators, respectively.

Existing WPT systems are based on the magnetic coupling of several tens of kilohertz to tens of megahertz frequency ranges. According to the different working frequencies, the desired physical quantities of BRs differed. At over 100 kHz, *ps*SAR and whole-body SAR were used as BRs to protect against adverse heating effects. Below 10 MHz, BR was defined as the induced electric field to shield from the stimulation effect. Therefore, the induced electric field and SARs must be considered within the range of 100 kHz to 10 MHz. The computation results for the magnetic-coupled WPT [101] suggested that under approximately 300–400 kHz, the induced electric field was more restrictive than *ps*SAR. Another study showed that the average whole-body SAR could be more dominant at higher frequencies [102]. However, variations in the whole-body average SAR could be high because it depends on the body weight, posture, the volume of the exposed body, coil size, materials, and source configuration [58], [103]. These issues require further investigations.

In our simulations, the separation between the torso and border of the resonator was set to 2 mm, which was much smaller than the generally used measurement distance (mostly 20 or 30 cm) specified in IEC 62233 for determining the electromagnetic field around household appliances [104]. Such standardization is currently being performed for WPT. Nonetheless, the calculated values could provide a rough (more conservative) estimate of the exposure doses of a WPT device with similar configurations.

3.5. Conclusion

In this study we proposed a modified resonator with a grounded loop for an MRC-WPT system to suppress electrical and magnetic stray field around WPT system and in consequence mitigate the interaction with the human body and obtain efficient short-range power transfers. The two systems' electromagnetic field distributions, performance, and human safety assessments were discussed and compared.

The full-wave simulation results demonstrated that the transmission efficiency improved in the proposed grounded resonator, which is a positive effect thanks to avoiding losses in human body. The strength of the stray electric field outside the grounded loop was reduced. The transmission efficiency was also insensitive to the proximity of the human body. Considering the interaction between the human body and the system, the grounded resonator reduced the exposure doses in the human body compared with the MRC-WPT with a non-grounded resonator.

The maximum induced electric field strength and the SAR values in the human body were reduced by 43.6% and 69.7%, respectively, using the proposed resonator. In the worst-case exposure scenario considered in this work, the maximum allowable input power was 33.5 kW when the grounded resonator was used in compliance with the prescribed ICNIRP limit for the whole-body averaged SAR, compared with 13.1 kW for the MRC-WPT with non-grounded resonators. The proposed resonators mentioned in the paper provide further information on the safe design of WPT systems. The resonator could be used in the future for electric vehicles and household applications.

Chapter 4

Reduction of Leakage Magnetic Field with Composite Core

4.1. Overview

The transmitting and receiving coils used in wireless power transfer (WPT) systems in electric vehicles (EVs) have a larger air gap (~300 mm) and higher transmission power (kW) than those in typical WPT systems used in electrical appliances. However, this could weaken the magnetic field, reduce transfer efficiency, and lead to public concern regarding potential adverse health effects related to electromagnetic field (EMF) exposure. Therefore, the assessment of compliance with product safety standards, based on international exposure guidelines such as the International Commission on Non-Ionizing Radiation Protection (ICNIRP), is crucial. The main goal of this study is to evaluate the performance of WPT systems used in EVs by using composite core materials and changing the core centre part design simultaneously to achieve improved transfer efficiency and enhanced magnetic field shielding. This study considers three types of planar ferrite cores for designing IPT systems for EVs. First, the transmission efficiency of the proposed WPT systems is calculated using the finite element method (FEM), where the vehicle body is not considered. Second, the magnetic field distribution of the system is compared with and without the vehicle model. In the exposure scenario of a human body standing near the vehicle, the scalar-potential-finite-difference (SPFD) method is used to assess the induced electric field in an anatomical human body to determine the assessed margin of exposure limits.

4.2. Method and Model

4.2.1. Geometric Structure of the EV-WPT System

Core-less system

In this Chapter, WPT system includes transmitting and receiving coils with identical structures. The transmitting and receiving coils form a “core-less” system, as shown in Figure 4.1 (a). Each comprises a double-layer coil made of Φ 4.6-mm copper litz wires with 20 (10 × 2) turns. The coils using litz wires can achieve high efficiency that can help mitigate skin and proximity effects, thereby minimizing losses owing to eddy AC currents [105]. The inner diameter of the coil is set to $d_{\mathrm{in\_coil}} = 82$ mm, and the outer diameter is set to $d_{\mathrm{out\_coil}} = 174$ mm. Also, when the coil is tightly wound, the minimum channel width of adjacent wires is zero. Moreover, the primary and secondary coils are initially separated by a distance of $h = 100$ mm, corresponding to the typical vehicle chassis height [106]. The system operational frequency is 85 kHz, which is in accordance with the EV wireless charging standard [23].

Core-based WPT system

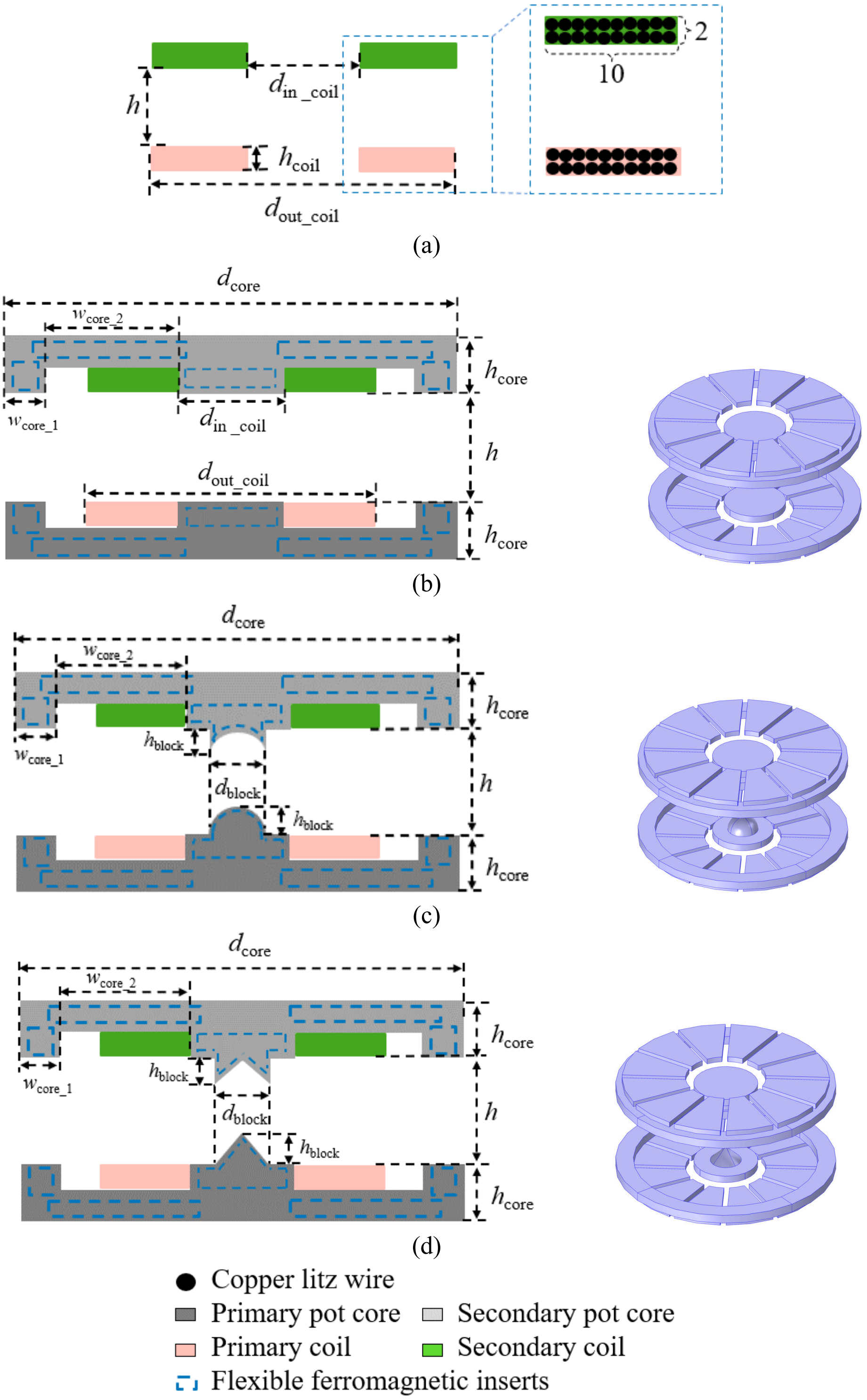

Figure 4.1 Geometry structure of the four wireless power transfer (WPT) systems and their insert structures (cross-section, unit: mm): (a) core-less, (b) core-based I, (c) core-based II, and (d) core-based III.

The pot core (core-based I), as shown in Figure 4.1 (b) was simulated and evaluated herein. Litz wires were used for fabricating transmitting and receiving coils, similar to those in the core-less system. The pot core shield is placed over the transmitting/receiving coils to reduce unwanted magnetic leakages [107]. To improve the mutual coefficient between the coils and divert magnetic flux lines from potential victims, flexible ferrite sheets were used as inserts and then embedded in the primary and secondary pot cores [108], [109]. The insert parts match the slots of the pot structures. In addition, the inserts can effectively improve the transfer efficiency [110]. The pot core and coils formed the primary and secondary parts of the system, respectively, and were of equal size [23]. The size of the cores was determined based on their geometry. To symmetrically and tightly settle the coils on the core surface, the core height is set to h_{core} = 14.4 mm. The protrusion with a width of $w_{\mathrm{core\_1}}$ = 5.5 mm on the outside of each core constrains the leakage field outside the coil and serves to collect the field and reduce leakage. For the core to cover the entire surface of the coils, the core notch width $w_{\mathrm{core\_2}}$ should be larger than the ring widths of the coils $((d_{\mathrm{out\_coil}} - d_{\mathrm{in\_coil}})/2)$ and equal to 70.4 mm. Also, the core diameter is larger than the outer diameter of the coils and is set to d_{core} = 270 mm.

Figure 4.1 (b) and (c) depicts the core-based II and III systems, respectively, showcasing their distinct center components compared to the core-based I system. The secondary part of the core-

Table 4.1 Size Values of the WPT System (Unit: mm)

d_{core}	d_{block}	$d_{\mathrm{in\_coil}}$	$d_{\mathrm{out\_coil}}$	$w_{\mathrm{core\_1}}$
270	41	82	174	70.4
h_{core}	h_{block}	h	h_{coil}	$w_{\mathrm{core\_2}}$
20	20.5	100	9.2	23.6

Table 4.2 Electromagnetic Properties of the Different Material Using in Simulation

Parameter	Relative Permittivity	Relative Permeability	Electrical Conductivity [S/m]
Coil	1	1	5.998×10^{7}
Core	2.8	9.5	5×10^{-13}
Insert	6.9	230	5×10^{-5}

based II system incorporates a hemispherical intermediate block, whereas the corresponding primary part has a hemispherical void. Similarly, the secondary part of the core-based III system uses a conical intermediate block, whereas the corresponding primary part has a conical void. The intermediate block diameter is set to d_{block} = 41 mm (= $d_{\text{in\_coil}}$/2). The intermediate block height is set to h_{block} = 20.5 mm, which is the same as the intermediate block radius (d_{block}/2). These complementary intermediate blocks are designed to alter the direction of magnetic flux lines. Also, using these specific geometric shapes, the core-based II and III systems aim at reducing magnetic field leakage and improving system performance. In addition, the system misalignment condition is also considered, as the scenario could possibly result in leaked magnetic field strength, corresponding to the worst-case exposure. The power loss in each proposed core has been computed as shown in Figure 4.2. The transferred power is set to 1 kW and the transmission distance to 100 mm. Table 4.1 summarizes the geometrical parameters of the four WPT systems. Moreover, Table 4.2 lists their electromagnetic parameters. The relative permittivity, relative permeability, and electrical conductivity with respect to the core along with the insert material

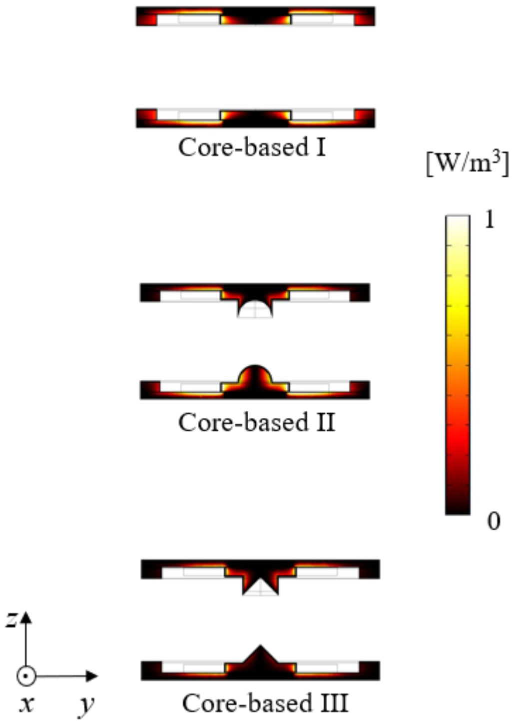

Figure 4.2 Power loss in each core of the 3 core-based WPT systems.

were measured at the LVSP Institute of Polymer Materials, Friedrich-Alexander-Universität Erlangen-Nürnberg (FAU) [111], [112]. In [111], the detailed production process of the core material is explained. From the paper, the hysteresis curves of the core material show almost perfect linear relation up to 9000 A/m at 50 Hz. In addition, the effectiveness of the material at 100 kHz is also shown at least up to 4000 A/m [111]. The computational results shown below will be within this range.

Equivalent Circuit of the WPT System with the Matching Circuit

In this study, the field-circuit co-simulation method was used to evaluate the proposed WPT system transfer efficiency using the commercial software COMSOL Multiphysics 6.0 [72], [74]. As shown in Figure 4.3, the power source can be modeled as a voltage source with internal resistance R_0 based on the Davidinan's theorem [113]. The transmitting and receiving coils in the system are characterized by internal resistance $R_{\text{Pri/Sec}}$ and self-inductances $L_{\text{Pri/Sec}}$ [5]. Furthermore, $R_{\text{Pri/Sec}}$ represents the ohmic losses of the coils. $L_{\text{Pri/Sec}}$ and $R_{\text{Pri/Sec}}$ are calculated using the frequency domain solver of the full-wave electromagnetic simulation package. The mutual inductance between the two coils is denoted as M, which connects the transmitter and receiver. The load resistance is set to 5 Ω [101]. Capacitors $C_{\text{Pri/Sec}}$ are introduced to resonate the transmitter and receiver at the desired frequency f_0, contributing to improved transfer efficiency [114]. $C_{\text{Pri/Sec}}$ is calculated as follows [45]:

$$C_{\text{Pri/Sec}} = \frac{1}{\omega_0{}^2 L_{\text{Pri/Sec}}} \tag{4.1}$$

where $\omega_0 = 2\pi f_0$, and $L_{\text{Pri/Sec}}$ is directly calculated using COMSOL.

In addition, one of the main challenges for WPT systems is to achieve an adequate level of power transfer efficiency as the distance between the transmitter and receiver varies. The L-shaped matching network, as the simplest network matching structure, is always used to overcome the mismatch problem [62]. As shown in Figure 4.3, an arbitrary complex load at port 1–1' ($Z_{in} = R_{in} + jX_{in}$) can be matched to the characteristic impedance R_0 (shown in Equation (4.2) by adjusting the parallel inductance L_m and the series capacitor C_m of matching network to achieve the maximum wireless power transfer efficiency.

$$\frac{1}{R_0} = j\frac{1}{\omega_0 L_m} + \frac{1}{R_{in} + jX_{in} + 1/j\omega_0 C_m} \tag{4.2}$$

The whole transfer efficiency η of the WPT system can be calculated can be expressed as follows:

$$\eta = \frac{P_{R_L}}{P_{in}} \tag{4.3}$$

Where P_{in} and P_{R_L} are the input power (at port 1–1') and load power (at port 2–2'), respectively. In practical applications, the system is more intricate, and other components are in [54].

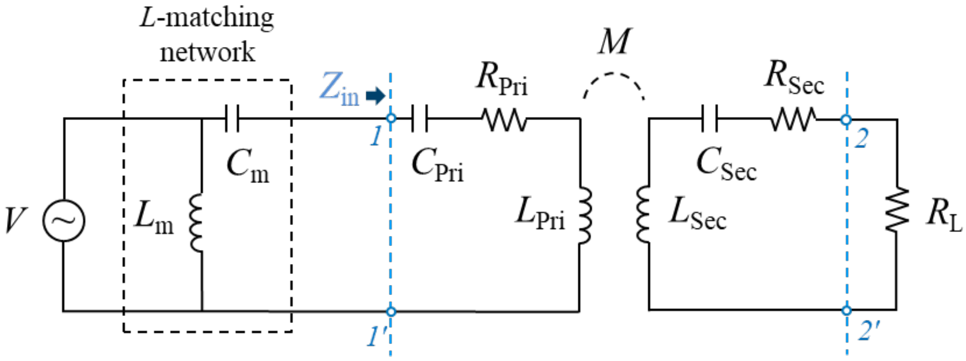

Figure 4.3 Equivalent circuit of the WPT system with the matching circuit ($\boldsymbol{R_{in}} < \boldsymbol{R_0}$).

4.2.2. Models and Exposure Scenario of the Simulation

Exposure Scenario

The light-blue rectangular as shown in Figure 4.4 is mentioned the exposure scenario in this study, where TARO was placed near the center of the vehicle with its lowermost point (feet) aligned with the horizontal position of the system transmitting coil. The front-facing aspect of TARO was directed toward the vehicle model while maintaining a separation distance of 200 mm [115]. All computational analyses were performed with respect to a constant power transfer of 1 kW at 85 kHz. For post-processing, the induced electric field of a 2 mm cube was evaluated, which is a metric described in the International Commission on Non-Ionizing Radiation Protection (ICNIRP) guidelines [116].

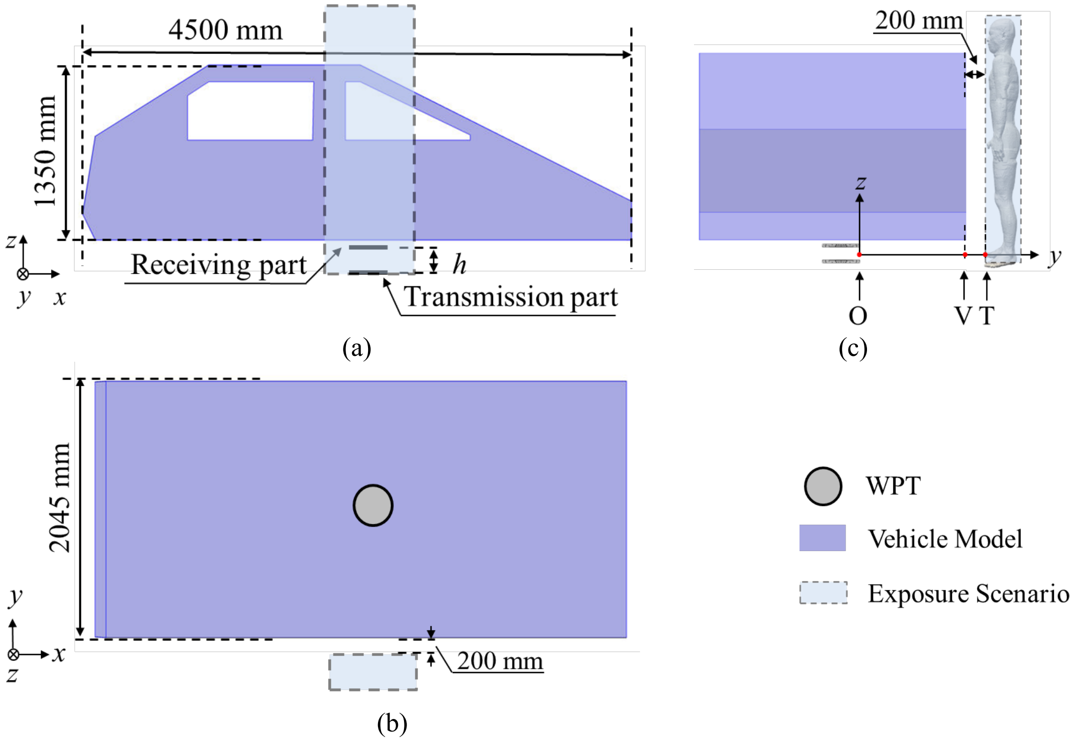

Figure 4.4 WPT location with respect to the vehicle cabin and TARO model: (a) xz-plane (b) xy-plane and (c) yz-plane. In Fig 5 (c), the point O represents the core-based system edge; point V represents the vehicle model location edge; and point T represents the start of the TARO model exposure scenario.

Simulation for Magnetic Field

Utilizing the methodology detailed in Section III-A, this investigation meticulously assessed both the transfer efficiency and magnetic field distribution of the proposed WPT system. To create a comprehensive simulation environment, the study defined the simulation domain as a sphere with a precisely specified radius of 2.5 meters. The discretization of this domain was achieved using tetrahedral meshes, and the mesh sizes were dynamically determined by the COMSOL software, ensuring an adaptive and accurate representation of the system.

Throughout the simulation runs, the chosen parameters remained constant, thereby ensuring the reproducibility and consistency of results in each calculation performed using COMSOL. Additionally, to examine the potential impact of increased granularity, finer settings were tested, revealing a negligible deviation of less than 1% from the original results. This experimentation underscores the robustness and reliability of the chosen discretization resolution.

Furthermore, to effectively confine the computational region, a perfectly matched layer was employed. This additional layer, implemented to truncate the computational domain, contributes to refining the simulation accuracy and maintaining computational stability throughout the evaluations.

The values of matching circuits L_m and C_m were calculated based on input and load resistances [113]. For the core-based I–III systems at the transmission distance h = 100 mm, C_m = 22.1, 25.7, and 26.4 μF, L_m = 26.6, 28.1, and 28.1 μH, respectively. By using the matching network, the power conversion efficiency of each system is 99.7%, 99.8%, and 99.8%, respectively.

As shown in Figure 4.4 [74], [117], the WPT system is installed below the vehicle body center with the receiving coil positioned at the end closest to the car chassis. At a transmission distance of 100 mm, the magnetic field distribution for each system with and without the vehicle model was initially compared with the perfectly aligned coils. Then, the effect of misalignment on the system with the vehicle model has been studied where the offset is set to Δy along the y-axis, positive direction.

Simulation of Exposure Doses in the TARO Model

A realistic anatomical human body model (TARO) was used to evaluate the induced electric field generated by stray magnetic fields using the proposed WPT systems. The magneto-quasi-static approximation can be used to compute the *in-situ* electric field when the frequency is lower than 10 MHz [36], [42].

Stray magnetic fields around the system and vehicle model were simulated using the FEM in the presence of the vehicle model. The resulting magnetic vector potential values were then calculated using COMSOL. Next, an in-house-developed solver created by Nagoya Institute of Technology (NITECH) based on the SPFD method was used to compute the induced electric field using the magnetic vector potential values serving as the source for computation [73]. This represented exposure to the external WPT magnetic field, wherein the presence of the human body model did not retroact on the external magnetic field distribution [26]. In addition, at low frequencies, the displacement current could be disregarded. This approach involves discretizing the computational target with cubical voxels and creating simultaneous linear equations for all contacts with the electric scalar potential serving as the unknown variable. The internal electric field is derived through matrix calculations, and the resulting matrix equation is solved using the geometric multigrid method.

4.3. Results

4.3.1. WPT System Performance

This research meticulously examines the transmission efficiency of each WPT system across varied transmission distances, spanning from 100 to 300 mm. For the sake of foundational discussion, the influence of the vehicle body is deliberately excluded from consideration in this section. As depicted in Figure 4.5 (a), the transmission efficiency of all WPT systems experiences a consistent decline with the augmentation of the transmission distance *h*. Notably, the outcomes reveal that WPT systems utilizing ferrite cores manifest superior transmission efficiency compared to their core-less counterparts.

The disparity in transmission efficiencies between the proposed system types becomes more pronounced as the transmission distance increases. Specifically, at a transmission distance of 300 mm, the transfer efficiency of core-based systems peaks at a level 34% higher than that of the core-less system. Simultaneously, a 4% elevation in maximum transmission efficiency is observed in core-based II and III systems relative to the core-based I system. Interestingly, despite having distinct intermediate blocks, core-based II and III systems exhibit nearly identical transmission efficiencies.

Considering the misalignment condition, Figure 4.5 (b) provides a comprehensive overview of the four systems under examination. Meanwhile, transmission distance is set to $h = 100$ mm and the offset of the primary part Δy is set from 0 to 250 mm, positive direction through the y-axis. As the misalignment distance widens, the transfer efficiency of the core-less system initially decreases and then experiences a temporary increase. Examining the core-based system, a discernible "valley" emerges in the proposed coil array between 120 to 180 mm misalignment distances. Beyond 200 mm misalignment distances, the transmission efficiency of the core-based I system is observed to be 5% lower than that of the core-based II and III systems.

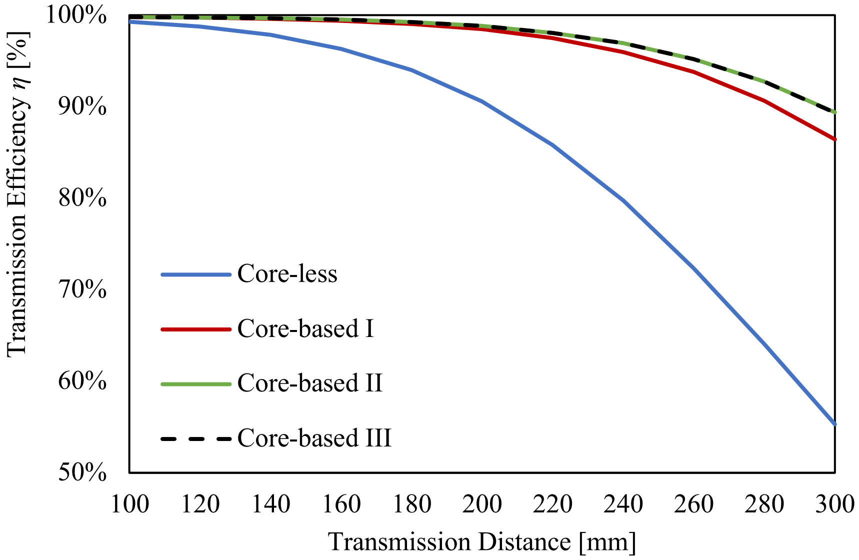

(a)

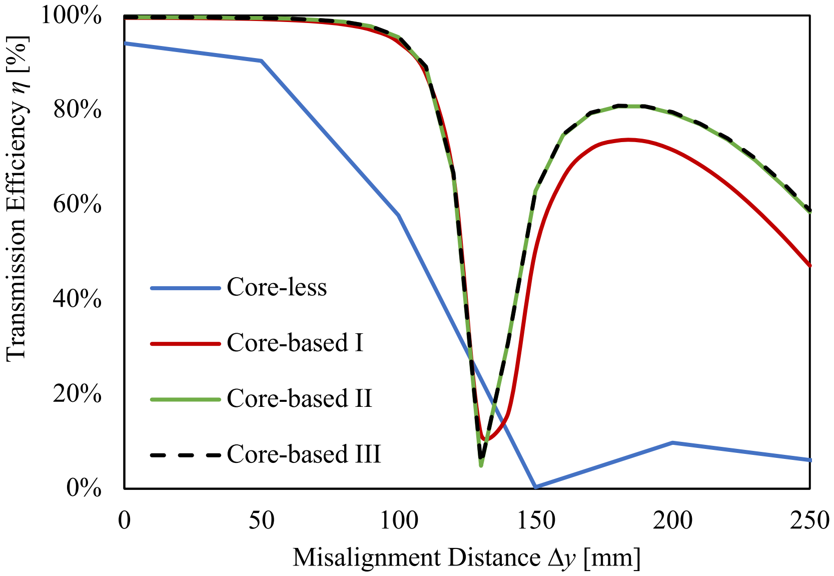

(b)

Figure 4.5 Transmission efficiency of four WPT systems variation with (a) transmission distance *h* and (b) misalignment distance Δy.

4.3.2. Magnetic Field Distribution

Herein, the magnetic field distributions of the four WPT systems are compared without considering the vehicle model. The results shown in Figure 4.6 indicate that the magnetic field distribution produced by the core-less WPT system has a wider range than that of the core-based systems. The core-less WPT system moderately exhibited strong magnetic field strength at the front and back sides of each coil. However, magnetic flux in the core-based systems is guided by the high magnetic permeability of the two cores, resulting in a substantial increase of magnetic field intensity between the two coils. In the three core-based WPT systems, the magnetic flux at the rear of the coils is restricted, indicating that the added core acts as a shield. Compared with the core-based I system, changes in the structural composition of the center part of the core-based II and III systems increase magnetic field intensity in the central region of the systems and the convergence of the external magnetic field range.

Figure 4.7 illustrates the magnetic field distribution of the four WPT systems in the presence of the vehicle model while the coils are perfectly aligned. The core-less WPT system produced the widest magnetic field distribution range underneath the vehicle model. Furthermore, the presence of cores in the core-based WPT systems reduced the magnetic field leakage range, with the core-based II and III systems exhibiting a smaller leakage range than the core-based I system.

Figure 4.8 shows the magnetic field strength of each system along the y-axis from point O as the coordinate origin (Figure 4.4 (b)) to the outside of the system while the transmission part and the receiving part are perfectly aligned. The results show that the magnetic field strength decreases gradually increasing the distance from the system, regardless of the presence or absence of the vehicle model. When only considering the system, the external magnetic field strength is initially nearly identical. However, as distance from the system increases, the magnetic field strength values with respect to the core-less and core-based I systems remain relatively consistent and higher than those with respect to the core-based II and III systems. The external magnetic field strength of the core-based II is marginally higher than that of the III system. Compared with the core-less and core-based I systems, the core-based II and III systems can reduce the external magnetic field intensity by 77.4% and 81.9% at point T, respectively. Although the core-based II and III systems have intermediate blocks, the magnetic field intensity of the core-based III system is lower than that of the core-based II system, demonstrating that modifications in the intermediate

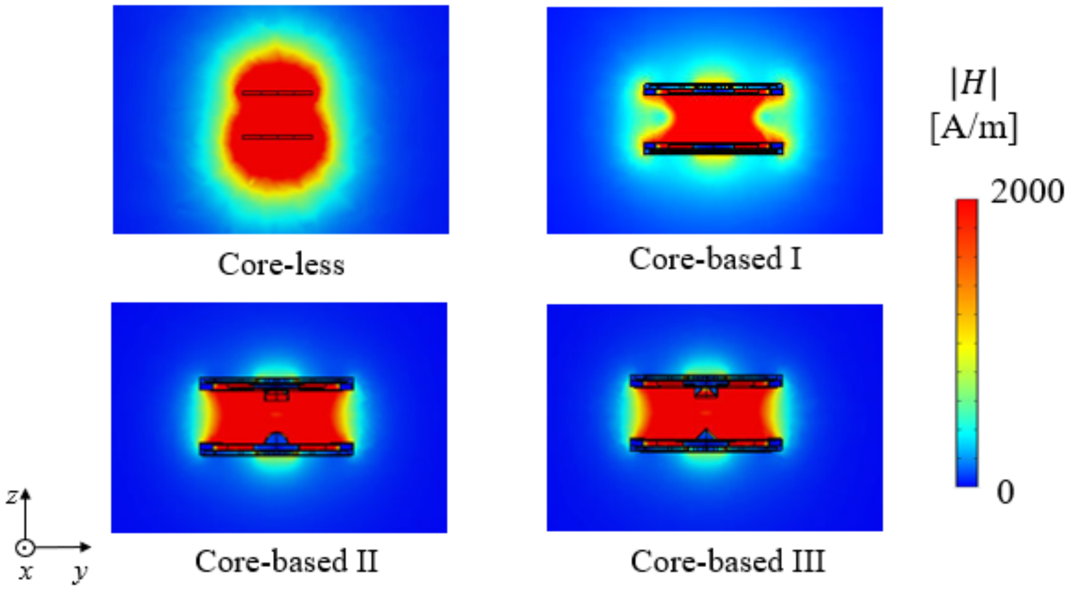

Figure 4.6 Magnetic field distribution (*H* [A/m]) for the cross-section of the perfectly aligned WPT models. The transferred power was set to 1 kW.

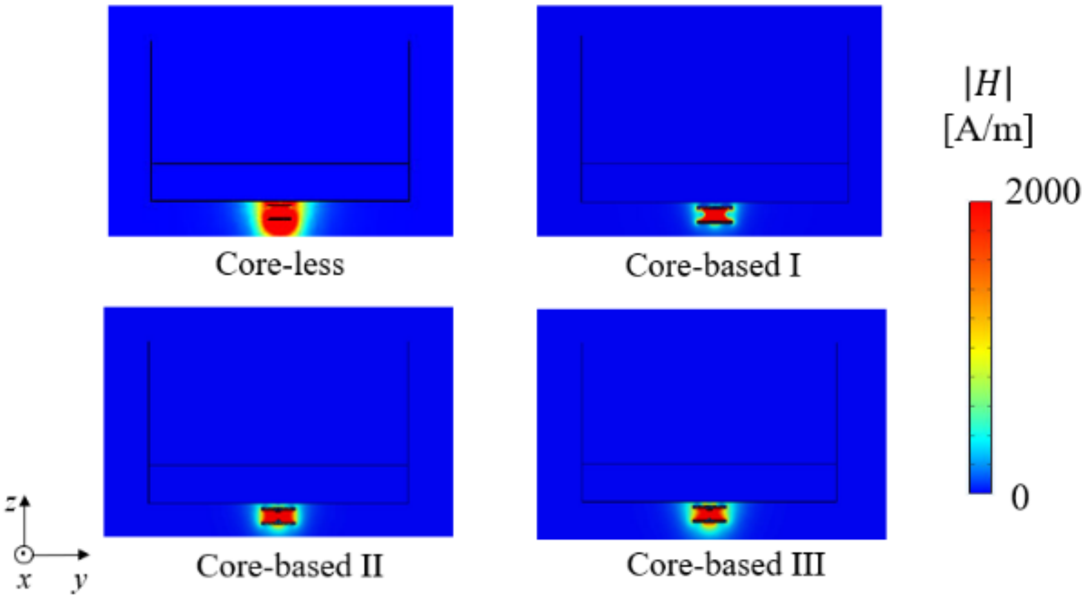

Figure 4.7 Magnetic field distribution (H [A/m]) for the cross-section of the perfectly aligned WPT models with the vehicle model. The transferred power was set to 1 kW.

block structure can reduce magnetic field leakage.

As depicted in the figure, the core-less system external magnetic field strength remains consistently higher than that of the other three core-based systems when considering the system with the vehicle model. Comparing the external magnetic field strength of the three core-based systems, core-based I exhibits higher values than the nearly identical values of core-based II and III. Comparatively, the core-based I–III systems can reduce the external magnetic field strength by a maximum of 64.8%, 91.5%, and 91.6%, respectively, compared with the core-less system at point T. According to the ICNIRP 2010 guidelines, the magnetic field limit for 3–100 kHz is 27 μT for public exposure. Following the magnetic field limit of ICNIRP, the maximum permissible

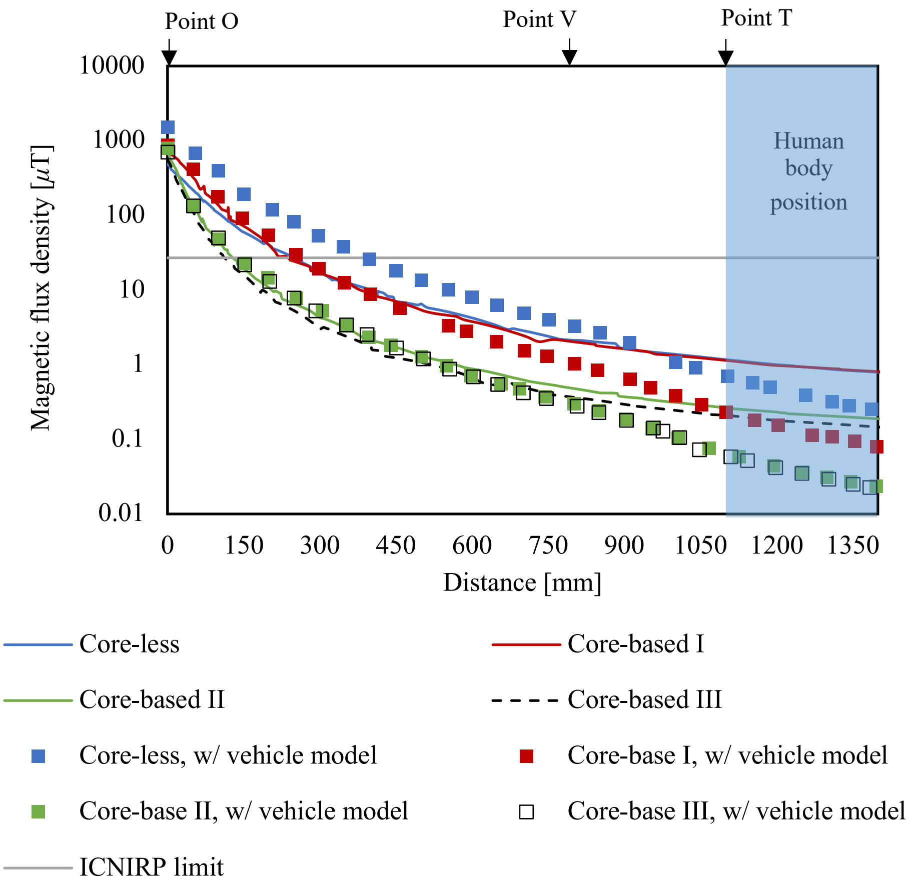

Figure 4.8 Comparison of the external magnetic flux density of four WPT systems with the limit of ICNIRP guidelines.

transferred power of the core-less and core-based I–III systems is 36, 108, 450, and 450 kW, respectively.

The magnetic field distribution of the three core-based systems were also studied with the misalignment condition. It was found that the misaligned distance Δy corresponds to a transfer efficiency of 95% in each core-based system [81]. Figure 4.9 illustrates the magnetic field distribution of the three core-based WPT systems, in the presence of the vehicle model. The value of Δy with core-based I–III systems is 96, 100, and 100 mm, respectively. As can be observed, the misalignment condition leads to an increase in the magnetic field strength.

Considering the perfectly aligned and misaligned conditions, Figure 4.10 shows the magnetic field strength of each core-based system along the y-axis from point O. The results show that magnetic field strength decreases gradually with increasing distance, observing nearly identical values for all three systems. The core-based I–III systems at the misalignment condition increased the external magnetic field strength by 81.5%, 93.3%, and 93.3%, respectively, compared with the perfectly aligned condition at point T. Following the magnetic field reference level of ICNIRP,

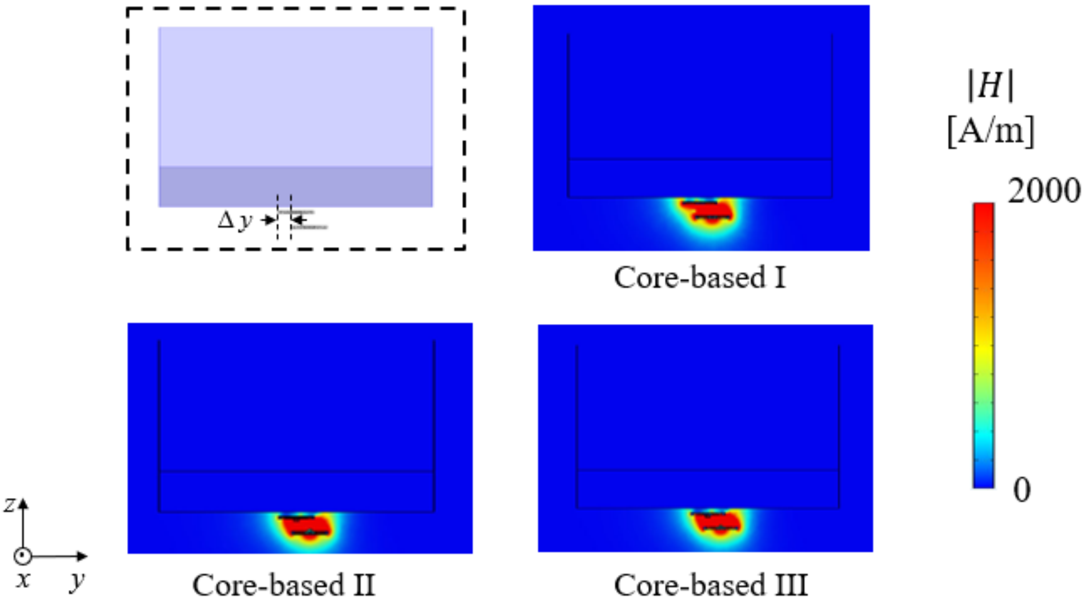

Figure 4.9 Magnetic field distribution (H [A/m]) on the misaligned WPT models with the vehicle cabin model cross-section. The transferred power was set to 1 kW and the misalignment distance Δy corresponds to a transfer efficiency of 95%.

the maximum permissible transferred power of the core-based I–III systems was 20, 24.3, and 24.3 kW, respectively.

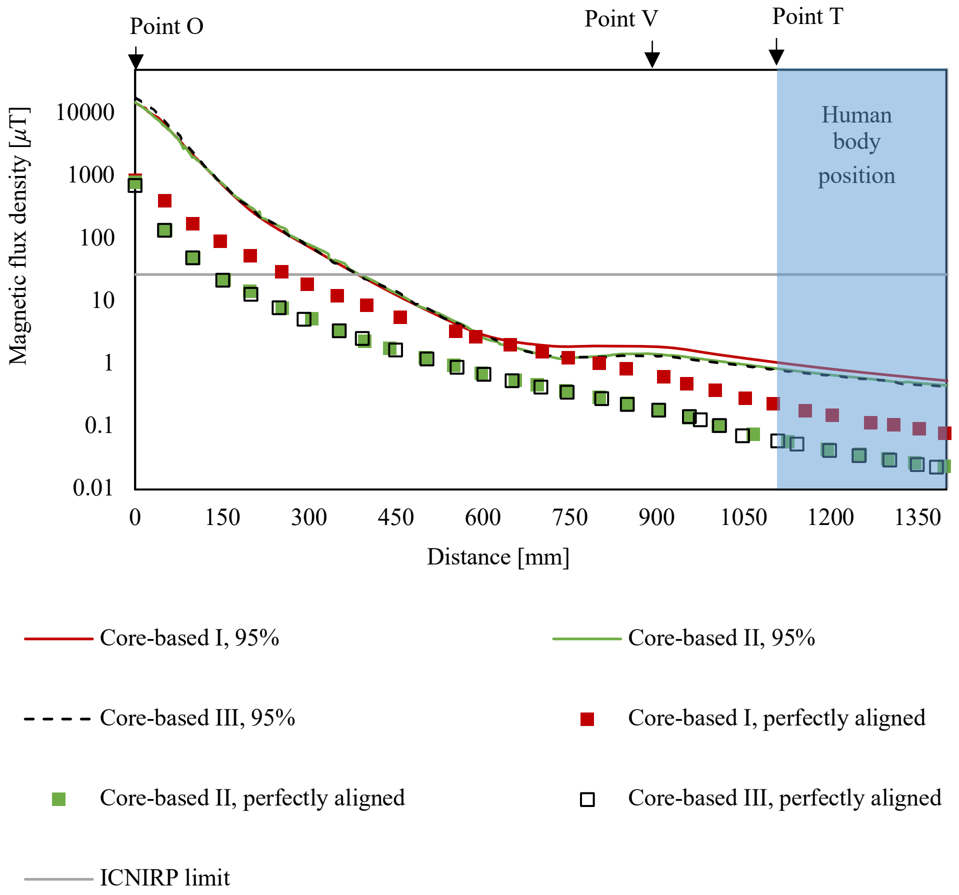

Figure 4.10 Comparison of the external magnetic flux density of three core-based WPT systems for the perfectly aligned and misaligned conditions with the limit of ICNIRP.

4.3.3. Induced Electric Field in the TARO Model

Figure 4.4 illustrates the WPT locations relative to TARO, where the distance in considering the vehicle model is set to 200 mm [115]. The simulation results, as shown in Figure 4.11 for the aligned and misaligned coil position, revealed that the WPT system with a core structure reduced the distribution and strength of the induced electric field in the TARO model. In all four perfectly aligned systems, being the parts of the body closest to the vehicle, hotspots appeared around the feet/lower legs, calves, and between the legs of TARO. However, when considering the three

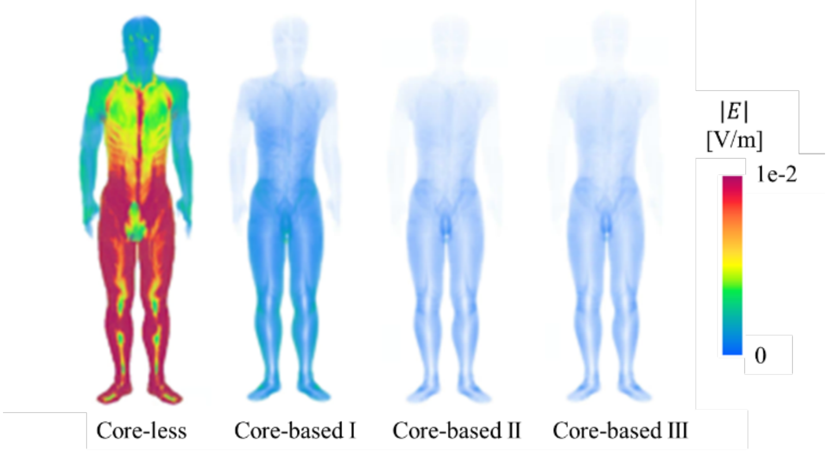

(a)

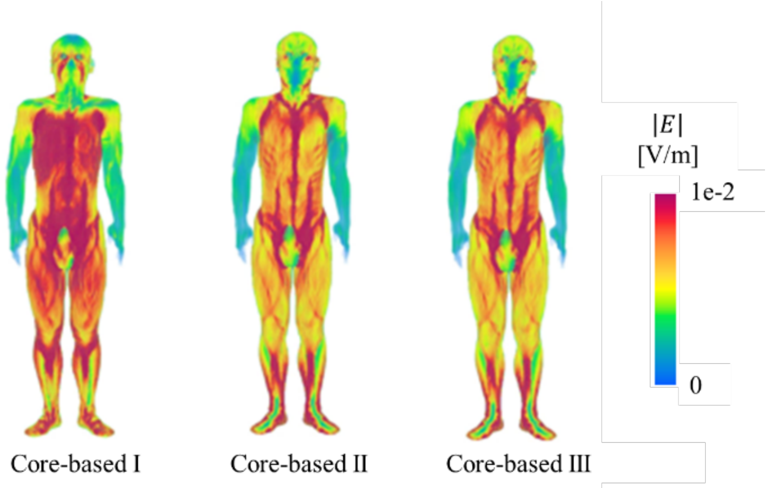

(b)

Figure 4.11 Distributions of induced electric field strength on the TARO model body surface (a) nearby the perfectly aligned system and (b) nearby the misalignment system.

core-based systems at the misalignment condition, hotspots appeared around the upper body. Furthermore, the WPT system with a core structure effectively reduced the intensity and spatial distribution of the electric field induced within the human body model. The WPT system core structure effectiveness varies, with the core-based II and III designs exhibiting greater reductions than the core-based I design in the induced electric field.

Table 4.3 lists the maximum induced electric field strength averaged over a 2 mm cube within the TARO model for the four WPT systems, with evaluations made for the perfectly aligned and misaligned cases. The results demonstrate superior performance by the three core-based WPT systems over the core-less WPT system in terms of reducing the induced electric field strength. Meanwhile, when considering the four systems at the perfectly aligned case, the core-based I–III systems exhibit reductions of 93.6%, 90.5%, and 98.3%, respectively, in the induced electric field strength compared with the core-less system. This reduction is primarily attributed to the core structure, which effectively suppresses electromagnetic field leakage around the WPT system.

Our computational value with 1 kW is scalable multiplying the induced electric field by multiply the ratio of the target transmitted power (kW value) to 1 kW. Considering the transferred power at 3.7 kW for the perfectly aligned case, the maximum induced electric field strength in this exposure scenario is 0.61 V/m for core-less, 0.038 V/m for core-based I, 0.011 V/m for core-based II, and 0.01 V/m for core-based III. Considering the transferred power at 11 kW for the perfectly aligned case, the maximum induced electric field strength in this exposure scenario is 1.82 V/m for core-less, 0.11 V/m for core-based I, 0.03 V/m for core-based II and core-based III. According to the ICNIRP 2010 guidelines, the induced electric field limit is 11.48 V/m for public exposure; the induced electric field in the body caused by the four systems is below 1% of the basic restriction when considering these two transferred power levels. Following this limit, the maximum permissible transferred power of the core-less was 69.6 kW, while core-based I–III system can be up to kW-level.

Considering the transferred power at 3.7 kW in the misalignment condition, the maximum induced electric field strength in this exposure scenario is 0.24 V/m for core-based I, 0.21 V/m for core-based II, and 0.2 V/m for core-based III. Considering the transferred power at 11 kW in the misalignment condition, the maximum induced electric field strength in this exposure scenario is 0.72 V/m for core-based I, 0.61 V/m for core-based II and core-based III. The induced electric field in the body caused by the three misaligned systems is below 1% of the basic restriction. Following the ICNIRP limit, the maximum permissible transferred power of the core-based I–III systems was 173, 206, and 207 kW, respectively.

Table 4.3 Maximum Values of the Induced Electric Field Strength (Unit: mV/m), the Misalignment Distance Corresponds to a Transfer Efficiency of 95%.

Case	Core-less	Core-based I	Core-based II	Core-based III
Perfectly aligned	165	10.4	3.13	2.83
Misaligned	N/A	66.2	55.7	55.6

4.4. Discussion

This study evaluated one core-less and three core-based WPT systems used for charging EVs. The evaluation criteria for these systems included transmission efficiency, leaked magnetic field intensity, and induced electric field in the anatomical human model placed near the vehicle. Moreover, this study considers two positional cases: perfectly aligned and misaligned.

Computational results obtained from full-wave simulations demonstrated that for the perfectly aligned case the transmission efficiency of these WPT systems decreased with increasing transmission distance, without considering the vehicle body model. This reduction in efficiency can be primarily attributed to the decrease in the coupling coefficient [118]. Furthermore, the core-based systems exhibited higher transmission efficiency than the core-less system. This is because the ferrite core in core-based systems can greatly divert magnetic flux lines, resulting in magnetic field concentration around the coils (Fig. 7) [112]. Moreover, the incorporation of hemispherical and conical intermediate blocks enhanced the ability of the systems to divert flux lines and reshape the magnetic distribution. Hence, these blocks reduce unwanted emissions and increase transmission efficiencies of the core-based II and III systems that are higher than that of the core-based I system. Overall, the proposed core system exhibits good performance, with a transmission efficiency exceeding 89% at a coil distance of 300 mm despite the core diameter of 270 mm. These results indicate that the proposed core design has been adapted to the system, as reducing core size is a critical factor in improving system efficiency while maintaining high-power transfer capability [47]. In addition, previous research has also been compared with this study, as shown in Table IV.

A transmission efficiency of 95% is often used as a misalignment condition that accounts for the above losses and uncertainties in practical EV-WPT systems [81]. It provides a margin for variations in alignment, environmental conditions, and system imperfections, ensuring that the system can still effectively function even under less-than-optimal conditions. In studying the variation of transmission efficiency in the presence of misalignment, we found that the proposed system is sensitive to misalignment. The “valley” phenomenon is generally owing to the varying effects of magnetic flux cancellation at different lateral displacements coupled with changes in the coupling coefficient.

Considering the perfectly aligned condition, the external magnetic field distribution and strength of the core-based systems were lower than the core-less system. The maximum magnetic field strength generated by the systems near the feet does not exceed the ICNIRP reference level, wherein the core-based systems achieved a maximum reduction of 91.6%, which is substantially lower than that of the core-less system. Hence, the induced electric field value generated by the external magnetic field in the TARO model is reduced by a maximum of 98.3%. These results indicate that the proposed core structure can reduce the adverse effects of EMFs generated by IPT systems on human health.

The magnetic field intensity range in the central region of the core-based II and III systems is enhanced compared to that of the core-based I system. This is because the direction of magnetic fluxes between the two coils is altered in the cases of systems II and III, causing external stray fluxes (especially around the core structures) to be substantially redirected toward the middle part of the system. Hence, the magnetic field strength between the coils increases, the magnetic field distribution range in the system central region expands, and the external magnetic field range converges, reducing magnetic field leakage. When considering the vehicle in studying the magnetic field distribution of the systems, structural changes in the center region of the core-based II and III systems altered the direction of magnetic fluxes toward the center of the system, reducing external magnetic field leakage. This finding is consistent with results related to the magnetic field distribution of the system without the vehicle model. Results in this study also reveal that the misalignment condition leads to the magnetic field level increase when compared to the perfectly aligned system. This finding is consistent with the observations in [98]. Moreover, core-based II and III shows more reduced this effect more than core-based I system for the misalignment condition.

Furthermore, even with similar magnetic field distributions and transmission efficiencies, the core-based III system exhibits greater reduction in external magnetic field strength and induced electric field value than the core-based II system, suggesting that core structure modifications can facilitate the design of safe WPT systems to improve safety during practical applications.

In the exposure scenario considered in this study, the maximum permissible transferred power calculated based on the ICNIRP limits of the induced electric field is 9.1 times higher than the maximum permissible transferred power calculated based on the magnetic field strength limits.

This disparity highlights the importance of evaluating induced electric fields when calculating permissible power transfer, which is also highlighted in the intercomparison of [105]. Moreover, the result obtained herein agrees with the result presented in that study.

The core structure presented herein can minimize the overall system volume and streamline the installation process compared with other shielding devices using WPT systems for charging EVs [38]. The primary reason for the differences among the core-based systems I–III is the distinct design of the core center. Although modifying the core center can reduce adverse effects on human health, this modification increases the weight and cost of the systems.

While it is beyond the scope of this study to discuss how implantable devices are affected, Hikage *et al.* [31] mentioned that the observed characteristics of the maximum interference distance of implantable devices depend upon the magnetic field distribution close to resonant WPT antennas and coil size. In addition, previous studies founded that the use of different materials/models can affect the magnetic field distribution inside and outside the vehicle body [56], [102], and the exposure conditions of child model deserve a separate discussion [121]. Moreover, the system operational frequency of this study is set to 85 kHz in accordance with the EV wireless charging standard [23], it should be mentioned that this material can be using at other frequency such as 110 kHz [112].

Despite the advantages of using IPT systems for charging EVs, some of its limitations need to be addressed in future research. For example, transmission distance may vary under different environmental conditions. Furthermore, considering the installation surroundings such as the possibility of uneven terrain or other equipment being simultaneously installed in the vehicle may affect the performance and safety of the system. A detector may also need to be considered in the system for animal protection from the application.

Table 4.4 Comparison of the Related Research

Year	2013 [100]	2015 [81]	2017 [48]	2018 [110]	2018 [65]	2018 [122]	2019 [43]	This study
Shield type	Rectangular core	N/A	Ferrite core + Aluminum plate	Ferromagnetic core + Aluminum plate	N/A	Ferrites tiles + Metal plate	Ferrite core + Aluminum shielding plate	Pot core + Magnetic material insert block
Operating Frequency	85 [kHz]	85 [kHz]	85 [kHz]	85 [kHz]	85 [kHz]	125 [kHz]	85 [kHz]	85 [kHz]
Max. Tx diameter /Length [mm]	405	405	600	600	500	600	500	270
Air gap [mm]	150	120	150	200	200	200	150	100
Transferred power [kW]	7	7	5	3.5	7.7	7.7	5	3.7
Efficiency at aligned case [%]	97.1	97.1	$k = 0.298$	96	$k = 0.07$	96	78	99.6
Magnetic field discussion	The averaged magnetic field strength that the model occupies is at most one half (adult models) or equal to (child) the reference level for the general public.	N/A	The magnetic flux density reduces by 25% for the optimized core configuration.	Reduced the magnetic flux density on the Rx core by about 44%.	Misalignment condition leads to an important increase of the magnetic field level.	The maximum magnetic field strength of the WPT system equipped with the ferrites was 28 A/m.	Reduced about 81% and 95% of the EMF average for the z-axis and x-axis, respectively.	Reduced the magnetic flux density on the human position up to 34%.
Human safety calculation	The maximal induced electric field in the body is at most 25% of the basic restriction.	The maximal induced electric field is 0.4 V/m.	N/A	N/A	Normalized to the peak value of induced electric field is 13.3 V/m for the aligned case; 19.9 V/m for misaligned case.	The maximal induced electric field is 0.42 V/m	N/A	The maximal induced electric field is 0.12 V/m
Considered exposure scenario	Human model is standing near to a vehicle model.	Human model is standing near to a vehicle model.			Human model inside the vehicle as driving passenger.	Human model is standing near the coil, human-coil distance is 235 mm.		Human model is standing near the vehicle, human-vehicle distance is 200 mm

4.5. Conclusion

In this study, three core structures with respect to efficient inductive WPT systems were considered to minimize magnetic field leakage. These core structures were evaluated against a core-less system in terms of efficiency without considering the vehicle model, leaked magnetic field strength, and induced electric field strength. Scenarios considering perfectly aligned and misaligned condition have been discussed. By concentrating on the magnetic field within the core structure and reducing its diffusion outside the system, EMF exposure was effectively reduced. For compliance assessment, a common exposure scenario, in which a human model stands near an EV, was considered. Using the proposed core structures, the results revealed a substantial reduction in the exposure doses of up to 90% with respect to the human body. The induced electric field within the body resulting from the proposed systems, under perfectly aligned and misaligned conditions, is below 1% of the basic restriction. Furthermore, the computation of this study showed that the proposed intermediate block within the core can further reduce magnetic field leakage and resultant adverse effects on the human body. This demonstrates the importance of designing a core structure with the aim of reducing EMF exposure from WPT systems to humans. However, the tradeoff between the improvements achieved and the associated increase in cost and weight owing to the core material used needs to be considered. Therefore, future research must focus on the proposed core structures for specific applications and consider the tradeoffs among efficiency, safety, cost, and weight. Experimental validation of the simulation results is also recommended to further improve the accuracy and reliability of the proposed WPT systems.

Chapter 5

Summary

In the realm of wireless power transfer (WPT) systems, particularly those adopting a non-radiative approach, their applications span a wide spectrum – from powering small devices to facilitating the energy needs of larger-scale equipment. Despite their evident advantages, these systems present challenges, notably in terms of ensuring human safety concerning electromagnetic fields (EMF) exposure and electromagnetic immunity. These concerns arise due to the potential health risks associated with the interaction between humans and the EMFs generated by these systems. As a response, international standards and guidelines have been established to address safety considerations, encompassing both industrial and human aspects. However, the dynamic nature of WPT technology necessitates ongoing research to evaluate and compare results against safety standards, ensuring continuous effectiveness while enabling efficient transmission.

This study leverages computer simulations to propose innovative WPT system designs, emphasizing high transmission efficiency, minimal human-system interaction, and reduced leakage field intensity. A magnetic resonant coupling WPT system, featuring a grounded loop, is introduced to enhance power transfer efficiency and mitigate human-system interaction. The simulation results demonstrate a transmission efficiency exceeding 70% at a transmission distance of approximately 25 cm, accompanied by a reduction in the electric field strength outside the grounded loop. Under conditions of maximum efficiency, the proposed loop achieves a noteworthy 43.6% reduction in induced electric field strength and a 69.7% reduction in SAR values. Importantly, the system complies with ICNIRP limits, even in worst-case exposure scenarios.

In the context of inductive coupling WPT systems for EV applications, a novel composite magnetic core is introduced to mitigate the impact of system magnetic field radiation on the surrounding environment while ensuring high efficiency. The study proposes three types of planar composite magnetic cores and evaluates their performances through finite-element method (FEM) simulations. Considerations extend to scenarios involving a misaligned EV model, where transmission efficiency and magnetic field distribution are assessed. Additionally, the study evaluates exposure scenarios for a human body near the vehicle, using the scalar-potential finite difference (SPFD) method to assess in-situ electric field exposure. The findings showcase a 34% improvement in transmission efficiency within a 30 cm air gap at perfect alignment, alongside substantial reductions of up to 91.6% in magnetic field leakage and 98.3% in induced electric field exposure. The proposed design enhances transmission efficiency and significantly mitigates human exposure to EMFs, aligning with ICNIRP limits for induced electric field exposure.

In total, the research underscores the importance of addressing not only the efficiency of wireless power transfer systems but also their impact on the surrounding environment and, crucially, human safety. The proposed magnetic resonant coupling and inductive coupling WPT systems, each with innovative design features, demonstrate significant improvements in efficiency and safety metrics.

The MRC-WPT system, incorporating a grounded loop, stands out for its ability to not only enhance power transfer efficiency but also to minimize human exposure to electromagnetic fields. The grounding of the loop contributes to a noteworthy reduction in electric field strength outside the loop, mitigating potential health risks associated with exposure. The systematic evaluation of induced electric field strength and SAR values showcases a substantial decrease under maximum efficiency conditions, aligning with stringent international safety standards.

On the other hand, the inductive coupling system, featuring a composite magnetic core, excels in mitigating the impact of magnetic field radiation on the environment. The proposed core structure, with an intermediate insert block, significantly reduces both magnetic field leakage and *in-situ* electric field exposure. This not only enhances transmission efficiency but also ensures compliance with exposure limits, emphasizing the safety of individuals in proximity to the system. Furthermore, this research investigates scenarios involving misalignment, providing insights into system performance under real-world conditions. The evaluation of transmission efficiency and magnetic field distribution during misalignment scenarios is crucial for practical applications, especially in the context of electric vehicles where perfect alignment is not always guaranteed.

In conclusion, the proposed designs present promising advancements in wireless power transfer technology, combining heightened efficiency with a steadfast commitment to environmental impact mitigation and human safety. These findings contribute to the ongoing discourse on shaping future WPT systems that not only meet energy transfer demands but also prioritize safety, sustainability, and compatibility with realistic conditions.

While significant progress has been made in WPT technology, applying these innovations to real-world scenarios requires deeper research to address a range of challenges. Enhancing system efficiency and minimizing human exposure considerations become more intricate, especially when accounting for various working conditions and environmental variables, such as different types of vehicles, complex road conditions, and diverse usage scenarios.

Furthermore, although existing international standards and guidelines provide safety benchmarks for WPT technology, the constant introduction and exploration of new materials necessitate a more thorough evaluation of the trade-off between technological advancements and factors such as material costs and weight. The introduction of new materials may bring performance improvements but could also lead to increased costs and weight, requiring a comprehensive consideration of these factors to find the optimal balance.

On the other hand, wireless charging systems can induce temperature increases in both devices and the human body. Future research should delve into understanding and addressing potential temperature dynamics issues, particularly in emerging technologies. Effectively managing temperature, preventing overheating, and mitigating adverse effects on devices and human health represent crucial directions for future research.

Lastly, as technology evolves, comprehensive research is needed to understand potential interference issues that wireless power transfer systems may cause to other electronic devices and communication systems. This encompasses ensuring the coexistence and interoperability of the system with surrounding devices to prevent conflicts or performance degradation in practical applications. Therefore, future research directions should focus on practical application details, utilizing in-depth field testing and validation to ensure the feasibility and reliability of these technologies in complex, real-world environments. This comprehensive research approach will further propel the development of wireless power transfer technology, ensuring its safety, high-efficiency, and practicality in real-world applications.

Acknowledgments

I would like to express my profound gratitude to my esteemed advisor, Prof. Akimasa Hirata, for his unwavering support throughout my Ph.D. journey and the associated research. His boundless patience, steadfast motivation, and extensive knowledge have been instrumental, guiding me meticulously through every step of the research and thesis writing process. His meticulous guidance has made my academic journey more vibrant and fruitful.

In addition to conveying my gratitude to Prof. Hirata, I extend my heartfelt appreciation for Prof. Georg Fischer, my co-supervisor, whose guidance has been invaluable during my research journey. Prof. Fischer has consistently offered novel insights, offering valuable guidance for my research. I am truly grateful for the warmth and encouragement he has extended to me.

Furthermore, I am sincerely appreciative of the esteemed members of my thesis committee: Prof. Jianqing Wang, Prof. Hiroshi Hirayama, and Prof. Takashi Hikage. Their insightful comments, unwavering encouragement, and thought-provoking questions have not only enriched my work but also encouraged me to approach my research from diverse perspectives.

I find myself deeply indebted to Prof. Masashi Hotta and Dr. Dr. Jens Kirchner for their invaluable support, which has been crucial to the success of my research endeavors. Their expertise and guidance have significantly shaped the quality and depth of my work.

My sincere appreciation also goes to Prof. Sachiko Kodera, Prof. Junqing Lan, Prof. Yinliang Diao and all the members of the laboratory for their significant contributions and unwavering support. Additionally, I express my heartfelt thanks to the Japan-Germany Research Internship Program (Grant No. 2019/R1) and the German Research Foundation's GRK2495/A project.

Finally, my heartfelt thanks go to my family and my friends in China, Japan, and Germany, for their continuous encouragement and unwavering support. Their steadfast belief in my abilities has been a constant source of strength throughout the entire research process, and I am profoundly grateful for their unwavering presence in my academic journey.

References

[1] K. M. Karakhanova, L. M. Kovyazin, and V. A. Trofimov, “Demonstration of the law of electromagnetic induction,” *Sov. Phys. - Uspekhi*, vol. 33, no. 3, pp. 253–254, 1990, doi: 10.1070/PU1990v033n03ABEH002554.

[2] A. A. Huurdeman, *The Worldwide History of Telecommunications*. Wiley, 2003.

[3] D. J. Cichon and W. Wiesbeck, “The Heinrich Hertz wireless experiments at Karlsruhe in the view of modern communication,” in *Proceedings of the 1995 International Conference on 100 Years of Radio*, 1995, pp. 1–6, doi: 10.1049/cp:19950782.

[4] N. Tesla, “Experiments with Alternate Currents of Very High Frequency and Their Application to Methods of Artificial Illumination,” *Lect. before Am. Inst. Electr. Eng.*, no. Columbia College, New York, p. ISBN 978-0809501625., 1891.

[5] A. Kurs, A. Karalis, R. Moffatt, J. D. Joannopoulos, P. Fisher, and M. Soljačić, “Wireless power transfer via strongly coupled magnetic resonances,” *Science*, vol. 317, no. 5834, pp. 83–86, 2007, doi: 10.1126/science.1143254.

[6] A. Mahesh, B. Chokkalingam, and L. Mihet-Popa, “Inductive Wireless Power Transfer Charging for Electric Vehicles-A Review,” *IEEE Access*, vol. 9, pp. 137667–137713, 2021, doi: 10.1109/ACCESS.2021.3116678.

[7] M. Scudiere and J. McKeever, “Wireless power transfer for electric vehicles,” *SAE Tech. Pap.*, 2011, doi: 10.1049/etr.2015.0017.

[8] S. Li and C. C. Mi, “Wireless Power Transfer for Electric Vehicle Applications,” *IEEE J. Emerg. Sel. Top. Power Electron.*, vol. 3, no. 1, pp. 4–17, 2015, doi: 10.1109/JESTPE.2014.2319453.

[9] H. Hoang, S. Lee, Y. Kim, Y. Choi, and F. Bien, “An adaptive technique to improve wireless power transfer for consumer electronics,” *IEEE Trans. Consum. Electron.*, vol. 58, no. 2, pp. 327–332, 2012, doi: 10.1109/TCE.2012.6227430.

[10] N. Van Thuan, S. H. Kang, J. H. Choi, and C. W. Jung, “Magnetic resonance wireless power transfer using three-coil system with single planar receiver for laptop applications,” *IEEE Trans. Consum. Electron.*, vol. 61, no. 2, pp. 160–166, 2015, doi: 10.1109/TCE.2015.7150569.

[11] S. Ding, S. Koulouridis, and L. Pichon, “Implantable wireless transmission rectenna system for biomedical wireless applications,” *IEEE Access*, vol. 8, pp. 195551–195558, 2020, doi: 10.1109/ACCESS.2020.3032848.

[12] M. Z. Bin Mustapa, S. Saat, Y. Yusof, and M. M. Shaari, “Capacitive power transfer in biomedical implantable device: a review,” *Int. J. Power Electron. Drive Syst.*, vol. 10, no. 2, p. 935, 2019, doi: 10.11591/ijpeds.v10.i2.pp935-942.

[13] A. M. Jawad, R. Nordin, S. K. Gharghan, H. M. Jawad, and M. Ismail, “Opportunities and challenges for near-field wireless power transfer: A review,” *Energies*, vol. 10, no. 7, pp. 1–28, 2017, doi: 10.3390/en10071022.

[14] V. Palazzi *et al.*, “Radiative Wireless Power Transfer: Where We Are and Where We Want to Go,” *IEEE Microw. Mag.*, vol. 24, no. 2, pp. 57–79, 2023, doi: 10.1109/MMM.2022.3210145.

[15] M. Henley, S. Potter, J. Howell, and J. Mankins, “Wireless Power Transmission Options for Space Solar Power,” *Int. Astronaut. Congr.*, p. IAC-02-R. 4.08, 2002.

[16] M. T. Nguyen *et al.*, *Electromagnetic field based WPT technologies for UAVs: A comprehensive survey*, vol. 9, no. 3. 2020.

[17] Z. Zhang, S. Zheng, Z. Yao, D. Xu, P. T. Krein, and H. Ma, “A Coil Positioning Method Integrated With an Orthogonal Decoupled Transformer for Inductive Power Transfer Systems,” *IEEE Trans. Power Electron.*, vol. 37, no. 8, pp. 9983–9998, 2022, doi: 10.1109/TPEL.2022.3155270.

[18] C. Lecluyse, B. Minnaert, and M. Kleemann, “A review of the current state of technology of capacitive wireless power transfer,” *Energies*, vol. 14, no. 18, pp. 1–22, 2021, doi: 10.3390/en14185862.

[19] I. Awai, “New theory for resonant-type wireless power transfer,” *IEEJ Trans. Electron. Inf. Syst.*, vol. 130, no. 6, pp. 966–971, 2010, doi: 10.1541/ieejeiss.130.966.

[20] Qi Standard, *Wireless Power Consortium*. https://www.wirelesspowerconsortium.com/.

[21] D. Van Wageningen and T. Staring, “The Qi wireless power standard,” *Proc. EPE-PEMC 2010 - 14th Int. Power Electron. Motion Control Conf.*, pp. S15-25-S15-32, 2010, doi: 10.1109/EPEPEMC.2010.5606673.

[22] AirFuel, “Wireless Charging Standards.” https://airfuel.org/wireless-charging-standards/.

[23] SAE J2954:2022, “Wireless Power Transfer for Light-Duty Plug-in/Electric Vehicles and Alignment Methodology,” no. August, p. 201, 2022, doi: 10.4271/J2954_202208.

[24] IEC 61980-1, “Electric vehicle wireless power transfer (WPT) systems - Part 1: General requirements,” *Int. Electrotech. Comm.*, 2020.

[25] IEC 61980-2, “Electric Vehicle Wireless Power Transfer (WPT) Systems—Part. 2: Specific Requirements for Communication between Electric Road Vehicle (EV) and Infrastructure,” *Int. Electrotech. Comm.*, 2023.

[26] IEC 61980-3, “Electric Vehicle Wireless Power Transfer (WPT) Systems—Part 3: Specific Requirements for the Magnetic Field Wireless Power Transfer Systems,” *Int. Electrotech. Comm.*, 2019.

[27] ISO 19363:2021, “Electrically propelled road vehicles - Magnetic field wireless power transfer - Safety and interoperability requirements,” *Int. Organ. Stand.*, pp. 1–41, 2021.

[28] L. Jiang, H. Liu, and C. Wang, “Summary of EMC Test Standards for Wireless Power Transfer Systems of Electric Vehicles,” *Proc. 2021 Asia-Pacific Int. Symp. Electromagn. Compat. APEMC 2021*, pp. 1–4, 2021, doi: 10.1109/APEMC49932.2021.9597175.

[29] ICNIRP, *Guidelines for limiting exposure to electromagnetic fields (100 kHz to 300 GHz)*, vol. 118, no. 5. 2020.

[30] IEEE, “IEEE Standard for Safety Levels with Respect to Human Exposure to Electric, Magnetic, and Electromagnetic Fields, 0 Hz to 300 GHz - Corrigenda 2,” *IEEE Std C95.1-2019/Cor2-2020 (Corrigenda to IEEE Std C95.1-2019)*, pp. 1–15, 2020, doi: 10.1109/IEEESTD.2020.9238523.

[31] G. Ziegelberger *et al.*, “Principles for non-ionizing radiation protection,” *Health Phys.*, vol. 118, no. 5, pp. 477–482, 2020, doi: 10.1097/HP.0000000000001252.

[32] C. E. Fernández-Rodríguez, A. A. A. De Salles, and D. L. Davis, “Dosimetric simulations of brain absorption of mobile phone radiation-the relationship between psSAR and age,” *IEEE Access*, vol. 3, pp. 2425–2430, 2015, doi: 10.1109/ACCESS.2015.2502900.

[33] T. Campi, S. Cruciani, F. Palandrani, V. De Santis, A. Hirata, and M. Feliziani, “Wireless Power Transfer Charging System for AIMDs and Pacemakers,” *IEEE Trans. Microw. Theory Tech.*, vol. 64, no. 2, pp. 633–642, 2016, doi: 10.1109/TMTT.2015.2511011.

[34] T. Arai and H. Hirayama, “Folded spiral resonator with double-layered structure for near-field wireless power transfer,” *Energies*, vol. 13, no. 7, 2020, doi: 10.3390/en13071581.

[35] A. Kumazawa, Y. Diao, A. Hirata, and H. Hirayama, “Reduction of Human Interaction with Wireless Power Transfer System Using Shielded Loop Coil,” *Electronics*, vol. 9, no. 6, p. 953, Jun. 2020, doi: 10.3390/electronics9060953.

[36] I. Laakso, S. Tsuchida, A. Hirata, and Y. Kamimura, “Evaluation of SAR in a human body model due to wireless power transmission in the 10MHz band,” *Phys. Med. Biol.*, vol. 57, no. 15, pp. 4991–5002, 2012, doi: 10.1088/0031-9155/57/15/4991.

[37] S. W. Park, “Misaligned effect and exposure assessment for wireless power transfer system using the anatomical whole-body human model,” *Prog. Electromagn. Res. C*, vol. 77, no. August, pp. 19–28, 2017, doi: 10.2528/PIERC17051909.

[38] T. Hikage, M. Yamagishi, K. Shindo, and T. Nojima, “Active implantable medical device EMI estimation for EV-charging WPT system based on 3D full-wave analysis,” *2017 Asia-Pacific Int. Symp. Electromagn. Compat. APEMC 2017*, pp. 87–89, 2017, doi: 10.1109/APEMC.2017.7975432.

[39] T. Campi, S. Cruciani, V. De Santis, F. Maradei, and M. Feliziani, “EMC and EMF safety issues in wireless charging system for an electric vehicle (EV),” *2017 Int. Conf. Electr. Electron. Technol. Automot.*, pp. 23–26, 2017, doi: 10.23919/EETA.2017.7993214.

[40] Y. L. Lyu *et al.*, “A Method of Using Nonidentical Resonant Coils for Frequency Splitting Elimination in Wireless Power Transfer,” *IEEE Trans. Power Electron.*, vol. 30, no. 11, pp. 6097–6107, 2015, doi: 10.1109/TPEL.2014.2387835.

[41] A. Hirata *et al.*, “Assessment of Human Exposure to Electromagnetic Fields: Review and Future Directions,” *IEEE Trans. Electromagn. Compat.*, vol. 63, no. 5, pp. 1619–1630, 2021, doi: 10.1109/TEMC.2021.3109249.

[42] A. Hirata, F. Ito, and I. Laakso, “Confirmation of quasi-static approximation in SAR evaluation for a wireless power transfer system,” *Phys. Med. Biol.*, vol. 58, no. 17, 2013, doi: 10.1088/0031-9155/58/17/N241.

[43] L. Tan, K. E. I. Elnail, M. Ju, and X. Huang, “Comparative analysis and design of the shielding techniques in WPT systems for charging EVs,” *Energies*, vol. 12, no. 11, pp. 1–20, 2019, doi: 10.3390/en12112115.

[44] W. Zhang, J. C. White, R. K. Malhan, and C. C. Mi, “Loosely Coupled Transformer Coil Design to Minimize EMF Radiation in Concerned Areas,” *IEEE Trans. Veh. Technol.*, vol. 65, no. 6, pp. 4779–4789, 2016, doi: 10.1109/TVT.2016.2535272.

[45] T. Campi, S. Cruciani, F. Maradei, and M. Feliziani, “Near-Field Reduction in a Wireless Power Transfer System Using LCC Compensation,” *IEEE Trans. Electromagn. Compat.*, vol. 59, no. 2, pp. 686–694, Apr. 2017, doi: 10.1109/TEMC.2016.2641383.

[46] T. Konstantinou *et al.*, “Feasibility Study and Design of In-Road Electric Vehicle Charging Technologies,” *Purdue Univ. Jt. Transp. Res. Progr.*, p. 51p, 2021, doi: 10.5703/1288284317353.

[47] G. A. Covic and J. T. Boys, “Modern trends in inductive power transfer for transportation applications,” *IEEE J. Emerg. Sel. Top. Power Electron.*, vol. 1, no. 1, pp. 28–41, 2013, doi: 10.1109/JESTPE.2013.2264473.

[48] M. Mohammad, S. Choi, M. Z. Islam, S. Kwak, and J. Baek, “Core design and optimization for better misalignment tolerance and higher range of wireless charging of PHEV,” *IEEE Trans. Transp. Electrif.*, vol. 3, no. 2, pp. 445–453, 2017, doi: 10.1109/TTE.2017.2663662.

[49] A. A. S. Mohamed, A. A. Shaier, H. Metwally, and S. I. Selem, “A comprehensive overview of inductive pad in electric vehicles stationary charging,” *Appl. Energy*, vol. 262, no. February, p. 114584, 2020, doi: 10.1016/j.apenergy.2020.114584.

[50] M. A. Houran, X. Yang, and W. Chen, “Magnetically coupled resonance wpt: Review of compensation topologies, resonator structures with misalignment, and emi diagnostics,” *Electron.*, vol. 7, no. 11, 2018, doi: 10.3390/electronics7110296.

[51] S. Kim, G. A. Covic, and J. T. Boys, “Tripolar Pad for Inductive Power Transfer Systems for EV Charging,” *IEEE Trans. Power Electron.*, vol. 32, no. 7, pp. 5045–5057, 2017, doi: 10.1109/TPEL.2016.2606893.

[52] A. A. La Mattina, S. Mariani, and G. Barillaro, “Bioresorbable Materials on the Rise: From Electronic Components and Physical Sensors to In Vivo Monitoring Systems,” *Adv. Sci.*, vol. 7, no. 4, 2020, doi: 10.1002/advs.201902872.

[53] T. Shijo, K. Ogawa, and S. Obayashi, “Optimization of thickness and shape of core block in resonator for 7 kW-class wireless power transfer system for PHEV/EV charging,” *2015 IEEE Energy Convers. Congr. Expo. ECCE 2015*, pp. 3099–3102, 2015, doi: 10.1109/ECCE.2015.7310094.

[54] E. R. Joy, A. Dalal, and P. Kumar, “Accurate computation of mutual inductance of two air core square coils with lateral and angular misalignments in a flat planar surface,” *IEEE Trans. Magn.*, vol. 50, no. 1, 2014, doi: 10.1109/TMAG.2013.2279130.

[55] N. S. A. Norodin, D. Sugita, and M. Hotta, “Study on Performance of 10 MHz Resonator-Coupling Type Wireless Power Transfer System with Some Misalignments,” *Proc. 19th IEEE Hiroshima Sect. Student Symp. (Matsue, Japan), A1*, no. February 2018, pp. 13–16, 2017.

[56] L. H. Hoang, R. Scorretti, N. Burais, and D. Voyer, “Numerical dosimetry of induced phenomena in the human body by a three-phase power line,” *IEEE Trans. Magn.*, vol. 45, no. 3, pp. 1666–1669, 2009, doi: 10.1109/TMAG.2009.2012771.

[57] I. Chatterjee, Y. G. Gu, and O. P. Gandhi, “Quantification of Electromagnetic Absorption in Humans from Body-Mounted Communication Transceivers,” *IEEE Trans. Veh. Technol.*, vol. 34, no. 2, pp. 55–62, 1985, doi: 10.1109/T-VT.1985.24037.

[58] T. Nagaoka *et al.*, “Development of realistic high-resolution whole-body voxel models of Japanese adult males and females of average height and weight, and application of models to radio-frequency electromagnetic-field dosimetry,” *Phys. Med. Biol.*, vol. 49, no. 1, pp. 1–15, 2004, doi: 10.1088/0031-9155/49/1/001.

[59] S. W. Park, “Investigating human exposure to a practical wireless power transfer system using and the effect about key parameters of dosimetry,” *PLoS One*, vol. 15, no. 8, pp. 1–21, 2020, doi: 10.1371/journal.pone.0236929.

[60] I. Laakso, T. Shimamoto, A. Hirata, and M. Feliziani, “Quasistatic approximation for exposure assessment of wireless power transfer,” *IEICE Trans. Commun.*, vol. E98B, no. 7, pp. 1156–1163, 2015, doi: 10.1587/transcom.E98.B.1156.

[61] A. Arduino *et al.*, “Accuracy Assessment of Numerical Dosimetry for the Evaluation of Human Exposure to Electric Vehicle Inductive Charging Systems,” *IEEE Trans. Electromagn. Compat.*, vol. 62, no. 5, pp. 1939–1950, 2020, doi: 10.1109/TEMC.2019.2954111.

[62] I. Laakso, A. Hirata, and O. Fujiwara, “Computational dosimetry for wireless charging of an electrical vehicle,” *IEEE Int. Symp. Electromagn. Compat.*, vol. 2014-Decem, pp. 202–205, 2014.

[63] A. Arduino *et al.*, “Numerical Aspects in Dosimetric Analysis of Human Exposure to Wireless Power Transfer for Electric Vehicles,” 2019.

[64] S. W. Park, K. Wake, and S. Watanabe, “Incident electric field effect and numerical dosimetry for a wireless power transfer system using magnetically coupled resonances,” *IEEE Trans. Microw. Theory Tech.*, vol. 61, no. 9, pp. 3461–3469, 2013, doi: 10.1109/TMTT.2013.2274053.

[65] V. De Santis, T. Campi, S. Cruciani, I. Laakso, and M. Feliziani, “Assessment of the induced electric fields in a carbon-fiber electrical vehicle equipped with a wireless power transfer system,” *Energies*, vol. 11, no. 3, 2018, doi: 10.3390/en11030684.

[66] A. Christ *et al.*, “Evaluation of Wireless Resonant Power Transfer Systems With Human Electromagnetic Exposure Limits,” *IEEE Trans. Electromagn. Compat.*, vol. 55, no. 2, pp. 265–274, 2013, doi: 10.1109/TEMC.2012.2219870.

[67] T. Shimamoto, M. Iwahashi, Y. Sugiyama, I. Laakso, A. Hirata, and T. Onishi, “SAR evaluation in models of an adult and a child for magnetic field from wireless power transfer systems at 6.78 MHz,” *Biomed. Phys. Eng. Express*, vol. 2, no. 2, 2016, doi: 10.1088/2057-1976/2/2/027001.

[68] T. Shimamoto, I. Laakso, and A. Hirata, “In-situ Electric Field for Human Body Model with Different Postures for Wireless Power Transfer System in an Electrical Vehicle,” *Phys. Med. Biol.*, vol. 60, pp. 163–173, 2015, doi: 10.1088/0031-9155/60/1/163.

[69] T. Campi, S. Cruciani, M. Feliziani, and A. Hirata, “Wireless power transfer system applied to an active implantable medical device,” *IEEE Wirel. Power Transf. Conf. 2014, IEEE WPTC 2014*, pp. 134–137, 2014, doi: 10.1109/WPT.2014.6839612.

[70] T. Sunohara, A. Hirata, I. Laakso, V. De Santis, and T. Onishi, “Evaluation of nonuniform field exposures with coupling factors,” *Phys. Med. Biol.*, vol. 60, no. 20, pp. 8129–8140, 2015, doi: 10.1088/0031-9155/60/20/8129.

[71] K. Wake *et al.*, “Derivation of Coupling Factors for Different Wireless Power Transfer Systems: Inter- and Intralaboratory Comparison,” *IEEE Trans. Electromagn. Compat.*, vol. 59, no. 2, pp. 677–685, 2017, doi: 10.1109/TEMC.2016.2636328.

[72] J. Pico, T. Bechtold, and D. Hohlfeld, “Model Order Reduction Using COMSOL Multiphysics ® Software - a Compact Model of a Wireless Power Transfer System,” *Proc. 2016 COMSOL Conf.*, pp. 4–6, 2016.

[73] I. Laakso and A. Hirata, “Fast multigrid-based computation of the induced electric field for transcranial magnetic stimulation,” *Phys. Med. Biol.*, vol. 57, no. 23, pp. 7753–7765, 2012, doi: 10.1088/0031-9155/57/23/7753.

[74] J. Lan and A. Hirata, “Effect of loudspeakers on the in situ electric field in a driver body model exposed to an electric vehicle wireless power transfer system,” *Energies*, vol. 13, no. 14, 2020, doi: 10.3390/en13143635.

[75] T. Campi, S. Cruciani, F. Maradei, and M. Feliziani, “Magnetic shielding design of wireless power transfer systems,” *Annu. Rev. Prog. Appl. Comput. Electromagn.*, vol. 2015-May, no. 1, pp. 422–425, 2015.

[76] C.-S. Wang, G. A. Covic, and O. H. Stielau, “Power transfer capability and bifurcation phenomena of loosely coupled inductive power transfer systems,” *IEEE Trans. Ind. Electron.*, vol. 51, no. 1, pp. 148–157, 2004, doi: 10.1109/TIE.2003.822038.

[77] H. A. Haus, “Waves and fields in optoelectronics,” *CEUR Workshop Proceedings*, vol. 897. 1984.

[78] IEC62233-2008, “Measurement methods for electromagnetic fields of household appliances and similar apparatus with regard to human exposure,” *Int. Electrotech. Comm.*, vol. 3, 2008.

[79] S. Gabriel, R. W. Lau, and C. Gabriel, “The dielectric properties of biological tissues: III. Parametric models for the dielectric spectrum of tissues,” *Phys. Med. Biol.*, vol. 41, no. 11, pp. 2271–2293, 1996.

[80] T. Kamiya, R. Onishi, S. Kodera, and A. Hirata, “Estimation of time-course core temperature and water loss in realistic adult and child models with urban micrometeorology prediction,” *Int. J. Environ. Res. Public Health*, vol. 16, no. 24, 2019, doi: 10.3390/ijerph16245097.

[81] T. Shimamoto, I. Laakso, and A. Hirata, “Internal electric field in pregnant-woman model for wireless power transfer systems in electric vehicles,” *Electron. Lett.*, vol. 51, no. 25, pp. 2136–2137, 2015, doi: 10.1049/el.2015.2457.

[82] K. Miwa, T. Takenaka, and A. Hirata, “Dosimetry and Compliance for Wireless Power Transfer Systems in Vehicle,” *Proc. 2020 Int. Symp. Electromagn. Compat. - EMC Eur. EMC Eur. 2020*, pp. 20–23, 2020, doi: 10.1109/EMCEUROPE48519.2020.9245849.

[83] A. Taflove, S. C. Hagness, and M. Piket-May, *Computational Electrodynamics: The Finite-Difference Time-Domain Method, Third Edition*. The Electrical Engineering Handbook, 2005.

[84] S. Gabriel, R. W. Lau, and C. Gabriel, “The dielectric properties of biological tissues: III. Parametric models for the dielectric spectrum of tissues,” *Phys. Med. Biol.*, vol. 41, no. 11, pp. 2251–2269, 1996, doi: 10.1088/0031-9155/41/11/003.

[85] K. Sasaki, K. Wake, and S. Watanabe, “Measurement of the dielectric properties of the epidermis and dermis at frequencies from 0.5GHz to 110GHz,” *Phys. Med. Biol.*, vol. 59, no. 16, pp. 4739–4747, 2014, doi: 10.1088/0031-9155/59/16/4739.

[86] K. Sasaki, M. Mizuno, K. Wake, and S. Watanabe, “Monte Carlo simulations of skin exposure to electromagnetic field from 10 GHz to 1 THz,” *Phys. Med. Biol.*, vol. 62, no. 17, pp. 6993–7010, 2017, doi: 10.1088/1361-6560/aa81fc.

[87] K. Li *et al.*, “Intercomparison of Calculated Incident Power Density and Temperature Rise for Exposure from Different Antennas at 10–90 GHz,” *IEEE Access*, vol. XX, pp. 1–1, 2021, doi: 10.1109/access.2021.3126738.

[88] “IEEE Recommended Practice for Measurements and Computations of Radio Frequency Electromagnetic Fields With Respect to Human Exposure to Such Fields,100 kHz-300 GHz,” *IEEE Std C95.3-2002 (Revision IEEE Std C95.3-1991)*, pp. i–126, 2002, doi: 10.1109/IEEESTD.2002.94226.

[89] X. Duan, N. S. A. Norodin, A. Sakata, and M. Hotta, “Fundamental Characteristics of Some Modified Shape Spiral-Resonators Used for Resonator-Coupled Type Wireless

Power Transfer System," *Proc. 21th IEEE Hiroshima Sect. Student Symp.*, no. 106, pp. 294–297, 2019.

[90] M. Hotta, N. S. A. Norodin, N. N. M. Zakaria, H. Onari, and T. Takegami, "Influence of lossy objects for resonator-coupled type wireless power transfer system with coplanar dual-spiral resonators," *Asia-Pacific Microw. Conf. Proceedings, APMC*, vol. 2018-Novem, pp. 40–42, 2019, doi: 10.23919/APMC.2018.8617132.

[91] G. Zhu, D. Gao, and S. Lin, "Leakage magnetic field suppression using dual-transmitter topology in EV wireless charging," *J. Power Electron.*, vol. 19, no. 3, pp. 625–636, 2019, doi: 10.6113/JPE.2019.19.3.625.

[92] Y. Li, R. Mai, T. Lin, H. Sun, and Z. He, "A novel WPT system based on dual transmitters and dual receivers for high power applications: Analysis, design and implementation," *Energies*, vol. 10, no. 2, 2017, doi: 10.3390/en10020174.

[93] S. Perhirin and Y. Auffret, "Influence of fields and SAR evaluation for 13.56 MHz EV resonance-based wireless power charging systems," *Microw. Opt. Technol. Lett.*, vol. 55, no. 11, pp. 2562–2568, 2013, doi: 10.1002/mop.

[94] R. Xue, K. Cheng, and M. Je, "High-Efficiency Wireless Power Transfer for Biomedical Implants by Optimal Resonant Load Transformation," *IEEE Trans. Circuits Syst. I Regul. Pap.*, vol. 60, no. 4, pp. 867–874, 2013, doi: 10.1109/TCSI.2012.2209297.

[95] H. Hirayama, T. Ozawa, Y. Hiraiwa, N. Kikuma, and K. Sakakibara, "A consideration of electro-magnetic-resonant coupling mode in wireless power transmission," *IEICE Electron. Express*, vol. 6, no. 19, pp. 1421–1425, 2009, doi: 10.1587/elex.6.1421.

[96] C. Kaufmann *et al.*, "Efficient frequency-transient co-simulation of coupled heat-electromagnetic problems," *J. Math. Ind.*, vol. 4, no. 1, pp. 1–3, 2014, doi: 10.1186/2190-5983-4-1.

[97] B. B. Tierney and A. Grbic, "Planar Shielded-Loop Resonators," *IEEE Trans. Antennas Propag.*, vol. 62, no. 6, pp. 3310–3320, 2014, doi: 10.1109/TAP.2014.2314305.

[98] I. Laakso, T. Uusitupa, and S. Ilvonen, "Comparison of SAR calculation algorithms for the finite-difference time-domain method," *Phys. Med. Biol.*, vol. 55, no. 15, p. N421, 2010.

[99] N. S. A. Norodin, K. Nakamura, and M. Hotta, "Effects of Lossy Mediums for Resonator-Coupled Type Wireless Power Transfer System using Conventional Single- and Dual-Spiral Resonators," *IEICE Trans. Electron.*, vol. 105, pp. 110–117, 2022.

[100] I. Laakso and A. Hirata, "Evaluation of the induced electric field and compliance procedure for a wireless power transfer system in an electrical vehicle," *Phys. Med. Biol.*, vol. 58, no. 21, pp. 7583–7593, 2013, doi: 10.1088/0031-9155/58/21/7583.

[101] X. Liu, C. Xia, and X. Yuan, "Study of the circular flat spiral coil structure effect on wireless power transfer system performance," *Energies*, vol. 11, no. 11, pp. 1–21, 2018, doi: 10.3390/en11112875.

[102] I. Dergham, Y. Alayli, R. Imad, and Y. Hamam, "Effects of a wireless charging system built for an electric kick scooter on human biological tissue," *Int. J. Environ. Res. Public Health*, vol. 17, no. 8, 2020, doi: 10.3390/ijerph17082662.

[103] V. De Santis, L. Giaccone, and F. Freschi, "Chassis influence on the exposure assessment of a compact ev during wpt recharging operations," *Magnetochemistry*, vol. 7, no. 2, pp. 1–11, 2021, doi: 10.3390/magnetochemistry7020025.

[104] IEC, "IEC 62233 : 2005 Measurement methods for electromagnetic fields of household appliances and similar apparatus with regard to human exposure," 2005.

[105] Y. Tang, H. Ma, D. J. Thrimawithana, and U. K. Madawala, "Copper foil windings for WPT systems," *2017 IEEE PELS Work. Emerg. Technol. Wirel. Power Transf. WoW 2017*, pp. 167–172, 2017, doi: 10.1109/WoW.2017.7959387.

[106] A. B. Diallo, M. Bensetti, C. Vollaire, L. Pichon, and A. Breard, "Scale Reduction for Modeling and Prototyping of Inductive Power Transfer System for EV Applications," *IEEE Trans. Magn.*, vol. 59, no. 5, pp. 1–4, 2023, doi: 10.1109/TMAG.2023.3239564.

[107] P. Vishnuram *et al.*, "Review of Wireless Charging System: Magnetic Materials, Coil Configurations, Challenges, and Future Perspectives," *Energies*, vol. 16, no. 10, 2023, doi: 10.3390/en16104020.

[108] Würth WE-FSFS Flexible Sintered Ferrite Sheet, https://uk.farnell.com/wefsfs-ferrite-sheet.

[109] WE-FSFS Flexible Sintered Ferrite Sheet. Accessed: Feb. 23, 2016. [Online]. Available: https://www.we-online.de/katalog/datasheet/ 354003.pdf, pp. 1–4.

[110] K. E. I. Elnail, X. Huang, C. Xiao, L. Tan, and X. Haozhe, "Core structure and electromagnetic field evaluation in WPT systems for charging electric vehicles," *Energies*, vol. 11, no. 7, pp. 1–17, 2018, doi: 10.3390/en11071734.

[111] D. W. Schubert, S. Werner, I. Hahn, and V. Solovieva, "Effect of particle size and size distribution on the permeability of soft magnetic liquid silicone rubber composites," *Compos. Sci. Technol.*, vol. 177, no. April, pp. 26–33, 2019, doi: 10.1016/j.compscitech.2019.04.005.

[112] H. F. Khalili *et al.*, “Transcutaneous Energy Transfer System for Cardiac-Assist Devices by Use of Inhomogeneous Biocompatible Core Material,” *IEEE Trans. Magn.*, vol. 57, no. 12, 2021, doi: 10.1109/TMAG.2021.3119235.

[113] Y. Lim, H. Tang, S. Lim, and J. Park, “An adaptive impedance-matching network based on a novel capacitor matrix for wireless power transfer,” *IEEE Trans. Power Electron.*, vol. 29, no. 8, pp. 4403–4413, 2014, doi: 10.1109/TPEL.2013.2292596.

[114] T. Campi, S. Cruciani, F. Maradei, and M. Feliziani, “Innovative Wireless Charging System for Implantable Capsule Robots,” *IEEE Trans. Electromagn. Compat.*, vol. 63, no. 5, pp. 1726–1734, 2021, doi: 10.1109/TEMC.2021.3078846.

[115] IEC 62764-1, “Determining procedures for the measurement of field levels generated by electronic and electrical equipment in the automotive environment with respect to human exposure,” 2022.

[116] ICNIRP: International Commission on Non-Ionizing Radiation Protection, “Guidelines for limiting exposure to time-varying electric and magnetic fields (1 Hz to 100 kHz),” *Health Phys.*, vol. 99, no. 6, pp. 818–836, 2010, doi: 10.1097/HP.0b013e3181f06c86.

[117] K. Miwa, T. Takenaka, and A. Hirata, “Electromagnetic Dosimetry and Compliance for Wireless Power Transfer Systems in Vehicles,” *IEEE Trans. Electromagn. Compat.*, vol. 61, no. 6, pp. 2024–2030, 2019, doi: 10.1109/TEMC.2019.2949983.

[118] I. Awai, Y. Zhang, T. Komori, and T. Ishizaki, “Coupling coefficient of spiral resonators used for wireless power transfer,” *Asia-Pacific Microw. Conf. Proceedings, APMC*, no. January 2010, pp. 1328–1331, 2010.

[119] T. Hikage, Y. Kawamura, T. Nojima, and E. Cabot, “Numerical assessment methodology for active implantable medical device EMI due to magnetic resonance wireless power transmission antenna,” *IEEE Int. Symp. Electromagn. Compat.*, pp. 1–6, 2012, doi: 10.1109/EMCEurope.2012.6396797.

[120] T. Campi, S. Cruciani, F. Maradei, and M. Feliziani, “Wireless Charging of Electric Vehicles: Planar Secondary Coil Position vs. Magnetic Field,” in *2019 International Symposium on Electromagnetic Compatibility - EMC EUROPE*, 2019, pp. 1116–1121, doi: 10.1109/EMCEurope.2019.8871775.

[121] J. F. Bakker *et al.*, “Children and adults exposed to low-frequency magnetic fields at the ICNIRP reference levels: Theoretical assessment of the induced electric fields,” *Phys. Med. Biol.*, vol. 57, no. 7, pp. 1815–1829, 2012, doi: 10.1088/0031-9155/57/7/1815.

[122] J. Chakarothai, K. Wake, T. Arima, S. Watanabe, and T. Uno, “Exposure Evaluation of an Actual Wireless Power Transfer System for an Electric Vehicle with Near-Field

Measurement," *IEEE Trans. Microw. Theory Tech.*, vol. 66, no. 3, pp. 1543–1552, 2018, doi: 10.1109/TMTT.2017.2748949.

Publication Lists

Published Papers for Thesis

i. X. Duan, J. Lan, Y. Diao, J. Gomez-Tames, H. Hirayama, M. Hotta, G. Fischer, and A. Hirata, “Reduction in Human Interaction with Magnetic Resonant Coupling WPT Systems with Grounded Loop”, Energies, vol. 14, no. 21, p. 7253, Nov. 2021, doi: 10.3390/en14217253. (査読あり)

ii. X. Duan, J. Lan, S. Kodera, J. Kirchner, G. Fischer, and A. Hirata, “Wireless Power Transfer Systems with Composite Cores for Magnetic Field Shielding with Electric Vehicles”, *IEEE Access*, vol. 11, pp. 144887-144901, 2023, doi:10.1109/ACCESS.2023.3344398. (査読あり)

Peer-Reviewed Journal Paper

iii. J. Lan, Y. Diao, X. Duan and A. Hirata, “Planar Omnidirectional Wireless Power Transfer System Based on Novel Metasurface,” IEEE Transactions on Electromagnetic Compatibility, vol. 64, no. 2, pp. 551-558, April 2022, doi: 10.1109/TEMC.2021.3123047.

Peer-Reviewed Conference Presentation for Thesis (Abstract)

iv. X. Duan, J. Lan, Y. Diao, J. Gomez-Tames, and A. Hirata, “A Magnetic Resonant Coupling Wireless Power Transfer System with Grounded Resonator to Reduce Interaction with Human Body”, BioEM 2021, PS-56, September 27, 2021.